

Microscopic Dynamics of Particle Rearrangement and its Correlation with Stick-slip Behavior in Granular Shear

Kwangmin Lee^a, Ryan C. Hurley^{a, b *}

^a *Department of Mechanical Engineering, Johns Hopkins University, Baltimore, Maryland 21218, USA*

^b *Hopkins Extreme Materials Institute, Johns Hopkins University, Baltimore, Maryland 21218, USA*

Abstract

The link between the microscopic dynamics of particles and the macroscale response of granular materials has not been well established. To address this, we investigated the microscopic dynamics and fluctuations in the force network in a granular material subjected to plane shear. A two-dimensional discrete element model of a plane shear test was established, considering both sliding and rolling friction. We found that particle rearrangement originated from the reduction of inter-particle forces in an identifiable region, which we call the greatest reduction (GR) region, defined as a region containing inter-particle forces experiencing the greatest decrease in magnitude in a given time interval. Statistical analysis shows that not only the magnitude of the greatest non-affine deformation in the GR region but also dynamics of neighboring particles in the region are highly correlated with the macroscale shear stress drop. These trends were also observed for various sliding friction coefficients and for simulations containing many particles. However, the quantity and configuration of GR regions had minimal impact on macroscale stress drops. We expect that this study will shed new light on the relationship between microscopic dynamics and force network fluctuations in sheared granular media and contribute to developing a mesoscale elasto-plastic model for these materials.

Keywords: Particle rearrangement; Stick-slip behavior; Shear transformation zone; Force network

* Corresponding author. Tel.: +1 410 516 5569

E-mail address: rhurley6@jhu.edu

1. Introduction

Particle rearrangements have been extensively investigated in granular materials because of the prevalence of these materials in industrial and geophysical processes, and in natural hazards such as earthquakes and landslides. However, particle rearrangements in disordered solids are challenging to understand and predict because the microscopic structure of these materials lacks long-range order, in contrast to crystalline materials. In crystalline materials, it is straightforward to detect a defect where the crystalline order is broken, and plasticity is typically initiated from certain types of these defects. The kinetics and kinematics of atoms around these defects, known as dislocations, have been well studied. On the other hand, the identification of defects and the resulting mechanical behavior of particle rearrangements in amorphous and granular materials have not been sufficiently studied.

Among prior research investigating particle rearrangement in granular and amorphous materials, there are broadly two approaches: those that seek to characterize the microscopic dynamics, and those that aim to investigate the force network. Taking the first approach, shear transformation zone (STZ) theories have been proposed. Argon, Spaepen, and others (Spaepen 1977; Argon 1979; Steif *et al.*, 1982) explained plastic deformation in metallic glasses through thermally-activated shear transformations initiated around free volume regions under an applied shear stress. Falk and Langer (1998) introduced the notion of STZs, local zones where rearrangements occur. To identify STZs, the same authors developed D^2_{\min} which measures the magnitude of local deviation from affine deformation. Langer (2001) established an analytical mean-field elastoplastic model (EPM), introducing STZs as zones with plastic deformation. In this model, a quadrupolar elastic displacement field is produced in the neighborhood of an STZ, and a corresponding change in the local stress fields occurs. Picard *et al.* (2004) advanced this understanding by specifically computing the long-range elastic perturbation induced by a localized plastic event in an elastic material. Considering this local relaxation, Picard *et al.* (2005) made an EPM for an amorphous material. Nicolas *et al.*, (2018) reviewed various EPMs for granular and amorphous solids. To predict particle rearrangements, correlation analysis with different structural indicators has been conducted to identify the structural defects responsible for plastic flow in amorphous solids (Cubuk *et al.*, 2015; Patinet *et al.*, 2016; Cubuk *et al.*, 2017; Barbot *et al.*, 2018; Richard *et al.*, 2020; Xu *et al.*, 2021; Ruan *et al.*, 2022; Stanifer and Manning, 2022; Zhai *et al.*, 2022).

Taking the second approach based on force networks, Cates *et al.* (1998) proposed a simple model to explain the jamming to unjamming transition based on force chains. Radjai *et al.* (1998) analyzed the correlation between contact forces and the texture of a packing of rigid particles using numerical simulations but did not specifically focus on rearrangements or unjamming. Peters *et al.* (2005)

characterized force chains in granular materials, providing a method for identifying force chains that was subsequently used for analyzing the behavior of granular materials. Tordesillas (2007) examined unjamming transitions and associated instabilities and particle rearrangements in dense granular systems using discrete element method (DEM) simulations. Tordesillas and Muthuswamy (2008) developed a multiscale thermo-micromechanical continuum model of dense granular materials considering force chain buckling. Tordesillas and Muthuswamy (2009) established an analytical model for force chain buckling and performed a parametric study to determine the effect of particle-scale properties on force chain stability. Using force chains and minimal contact cycles, Tordesillas *et al.* (2011) studied the evolving stability of jammed states of specific cluster conformations, *i.e.*, particles forming force chains and minimal contact cycles in dense granular materials. Kramer *et al.* (2022) and Bretz *et al.* (2023) found that using the average of local measures including the persistence diagram of force networks, differential force network, and broken, mobile, and nonmobile contacts, the time when macroscale slip occurs can be predicted. Although the two approaches of analyzing microscopic dynamics and force networks are complementary, there is a lack of research connecting the two methodologies. In particular, studies integrating the concepts of STZs and force networks to comprehensively understand the behavior of granular materials have been relatively rare.

Recently, Ma *et al.* (2021) studied the initialization and localization of plastic events within various timescales. They found that there is a moderate correlation between D^2_{\min} and local stress fluctuations in sheared granular media, indicating that non-affine deformations originated at particles experiencing significant stress fluctuations over short time scales. Ma *et al.* (2022) and Mei *et al.* (2022, 2023) predicted macroscale stress fluctuations based on the D^2_{\min} distribution field with machine learning. They found that, during the slip event, the microscopic dynamics are more spatially concentrated and tend to generate large clusters inside the granular system. Although their predictions were accurate, quantifiable links between individual-particle dynamics and the macroscopic response of granular materials were not well established due to the black box nature of machine learning.

This work aims to investigate the relationship between microscopic dynamics and force network fluctuations associated with particle rearrangements in sheared granular media. The ultimate goal of this work is to establish quantifiable links between the microscopic dynamics and kinetics of particles and the macroscale response of granular materials. To achieve this, we established a 2D DEM model of a plane shear test considering both sliding and rolling friction. We found that the weakening of a clustered set of inter-particle forces, which we term the greatest reduction (GR) region, is the origin of particle rearrangement. Correlation analysis shows that the magnitude of the greatest non-affine deformation in the

GR region, as quantified by the D_{\min}^2 metric, as well as the structure of neighboring particles of that point, influences the macroscale shear stress drop. On the other hand, the shape and number of GR regions do not significantly affect macroscopic stress fluctuations. We expect that our research will contribute to the understanding of particle rearrangements and aid in developing an EPM in granular materials.

The remainder of the paper is structured as follows. Section 2 introduces the DEM model used for plane shear simulations. Section 3 discusses DEM results first for a small sample containing around 1,000 particles. For this sample, non-affine particle dynamics and GR regions are analyzed in detail to demonstrate strong correlations between the two. Section 4 discusses an expansion of DEM simulations to other friction coefficients, while Section 5 discusses correlation between non-affine particle dynamics and GR regions for larger samples containing many thousands of particles. Section 6 offers a discussion and Section 7 provides concluding remarks.

2. Discrete element method (DEM) model

We first created a two-dimensional DEM model for a plane shear test (Fig. 1). The DEM code used for this was LIGGGHTS (version 3.8.0) (Kloss *et al.*, 2012). For particle size, $0.5\text{-}1\text{ }\mu\text{m}$ with uniform distribution was chosen for the radius of the particles. The number of particles was around 1,000. Here, a small number of particles was chosen to study the movement and interaction of each particle in more detail. However, simulations containing more particles were also conducted and demonstrated similar qualitative responses; the results of these simulations are discussed in Section 5. For boundary conditions, the particles constituting the bottom boundary were fixed, while particles constituting the upper particles were velocity-controlled to apply a constant normal force, N , as well as a constant shear velocity, V . Particles constituting the upper wall were constrained to move together and their positions were integrated using a velocity-Verlet scheme. The mass of the top wall is the sum of the masses of the particles that constitute it. Particles between the walls were integrated using a velocity-Verlet scheme, and gravity was neglected in all calculations. The sample's normal force, N , and shear force, S , are the sum of the normal and shear forces acting on the particles constituting the top boundary, respectively. We chose 4×10^{-6} for the inertial number, I , and thus simulations were in the quasi-static regime (da Cruz *et al.*, 2005). We chose 10,000 for the contact stiffness number, κ , and thus simulations were in the elastic and stiff-particle regime in which particle stiffness does not qualitatively influence results (da Cruz *et al.*, 2005). For the normal and tangential contact models, the Hertz contact model for cylindrical bodies (Johnson, 1985) and Lai *et al.*'s semi-analytical Hertzian frictional model in two dimensions (2021) were used, respectively, both incorporating the linear damping models (Hu *et al.*, 2011). For the rolling resistance model, the type C elastic-plastic spring-dashpot model

(Ai *et al.*, 2011) was employed. Appendix A provides a detailed description of the contact models. For materials properties, 1 GPa, 0.2, 0.9, and 2500 kg / m³ were chosen for Young's modulus, Poisson's ratio, coefficient of restitution, and density, respectively. For sliding friction coefficients, μ_s , and rolling friction coefficients, μ_r , 0.7 and 0.01 were used, respectively. Here, we assumed that the particle shape is circular and the actual contact moment is negligible, and thus a significantly small value was chosen for μ_r . The contact moment introduced in this DEM model is an artificial means of capturing the effect of particle shape irregularities. The simulations for various μ_s were also conducted and the results are given in Section 4. For damping constants at the contact, 0.1, 0.1, and 0.3 were chosen for viscoelastic damping constant for normal force, γ_n , viscoelastic damping constant for tangential force, γ_t , and rolling viscous damping ratio, η_r , respectively.

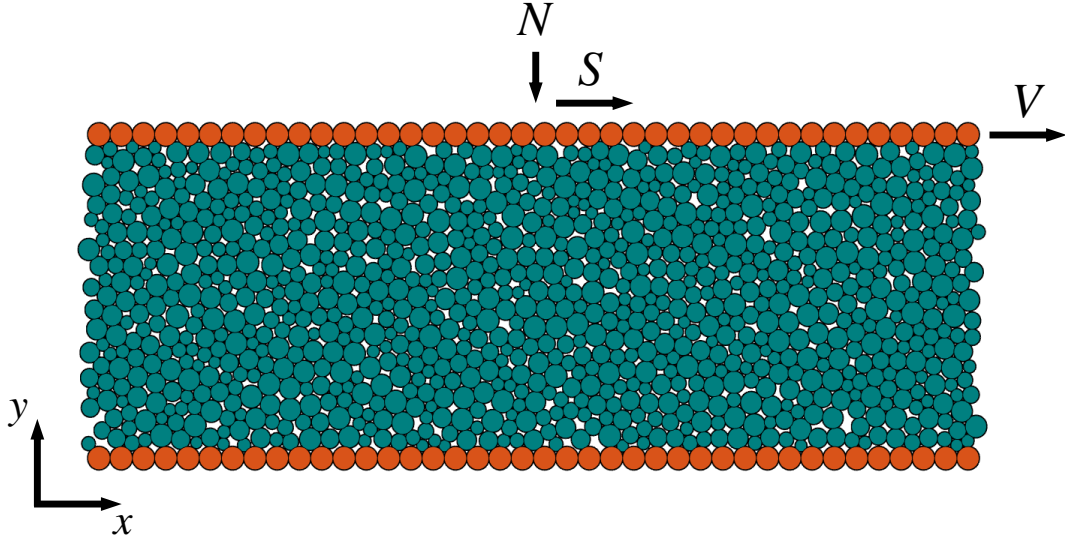


Fig. 1. DEM model for a plane shear test.

3. DEM results

3.1. Macroscopic response

The normalized shear stress-strain curve is shown in Fig. 2a. The normalized shear stress, τ , is defined as the ratio of shear to normal force, S / N , measured in the sheared granular material, as described in Section 2.

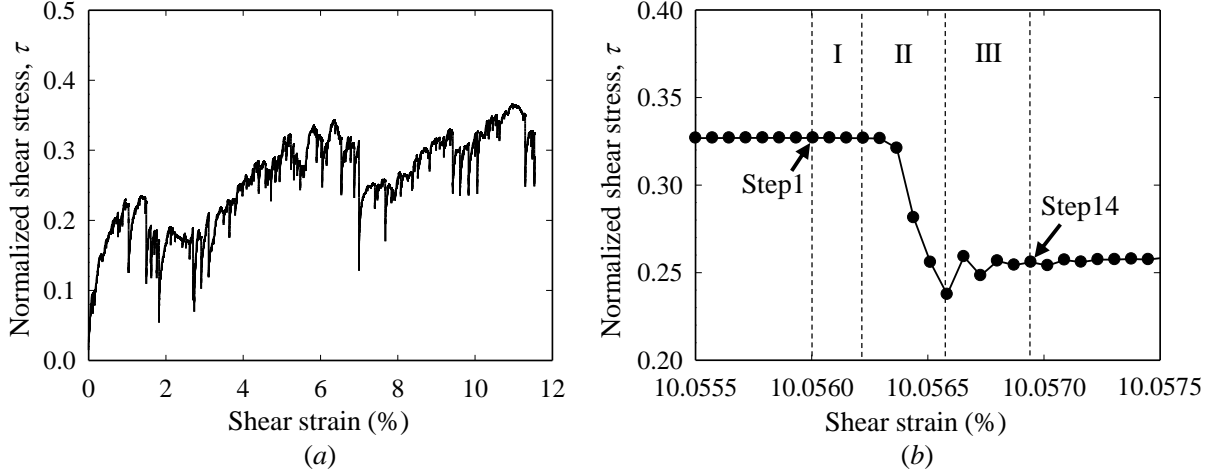


Fig. 2: (a) Normalized shear stress-strain curve from discrete element method simulation. (b) Normalized shear stress-strain curve around a slip event occurring between 10.0555% to 10.0575% shear strain; the region around the slip event is delineated into three distinct stages: the pre-stress drop stage (Stage I), the stress drop stage (Stage II), and the post-stress drop stage (Stage III).

3.2. Microscopic dynamics and force network analysis around slip event

During the shearing process, we observed a total of approximately 42,000 phases in the stick-slip regime (shear strain $\geq 2.2\%$), where each phase comprises both stick (ascending) and slip (descending) stress fluctuation events in the normalized shear stress-strain curve. A stick event (or stick phase) starts when τ increases and ends when this increase ends. In contrast, a slip event (or slip phase) begins when τ decreases and ends when this decrease ends. In the shear stress-strain curve depicted in Fig. 2a, the stick-slip regime is identified as the region where the shear strain exceeds 2.2%. While 2.2% does not clearly reflect a critical state in Fig. 2a, the choice to analyze this region reflects the observation of significant stick-slip after 2.2% strain, permits analysis of many phases, and leads to qualitatively similar results to those shown in Sec. 5, where a critical state is more clearly identifiable. To provide insight into the nature of these events, we first focused on the region around the largest stress drop observed in the stick-slip regime, specifically between 10.0555% to 10.0575% shear strain as depicted in Fig. 2b. This region around the slip event is divided into three stages based on the macroscale shear stress profile: the pre-stress drop stage (Stage I), which is the period before the significant stress reduction begins; the stress drop stage (Stage II), characterized by the largest decrease in stress; and the post-stress drop stage (Stage III), which is the period immediately following the stress drop stage. This region was studied at the particle scale based on the force network, differential force network, D^2_{\min} field (a measure of the magnitude of local non-affine deformation), and non-affine displacement field. The D^2_{\min} was computed based on the definition in Mei *et al.*, 2023 with a

local averaging region of radius $r = 5r_p$, where r_p is the average radius of particles. The details of the D^2_{\min} computation can be found in Appendix B. The macroscale shear strain increments between which inter-particle forces and particle positions were output from the DEM simulation, $\Delta\gamma$, was 7.2×10^{-7} for this analysis.

Figures 3-5 show the particles experiencing the greatest 1% reduction in inter-particle force magnitude, the differential force network at each $\Delta\gamma$ increment, the particles experiencing the greatest 1% D^2_{\min} magnitude, and the D^2_{\min} magnitudes in Stages I-III during 10.0555 - 10.0575% shear strain in Fig. 2b. The steps noted in Figs. 3-5 are detailed in Fig. 2b. Here, the differential force network is calculated as $f^\alpha_t - f^\alpha_{t-1}$ of each contact α , where f^α_t and f^α_{t-1} are the magnitudes of inter-particle force vectors at the current time step and previous time step (separated by a strain increment of 7.2×10^{-7}), respectively. If the force bearing contacts at the previous time step are created or destroyed at the current time step, its differential force network is set to zero. In theory, an STZ can be considered a local plasticity event; on the other hand, an STZ can also be a group of particles within loosely packed regions undergoing a change in configuration, which are known as rattler particles. In this study, rattler particles are defined as particles inside the sample that have two or fewer inter-particle contacts, and particles in the top or bottom walls that have one or fewer inter-particle contacts. Because these rattler particles are not involved in the plastic event, they were excluded from the computation of D^2_{\min} . The colorless disks in the D^2_{\min} graphs in the right-most columns of Figures 3-5 represent the rattler particles. Figure 6 shows the force network in Stages I-III.

Before the stress drop occurred in Stage I, both the differential forces and D^2_{\min} were somewhat randomly distributed spatially, though initial signs of concentration towards a single region were already observed (Fig. 3). At the beginning of Stage II, the locations of the greatest differential force decrease further concentrated towards a single region (right lower part of the sample) and made a single cluster (Steps 4-5) (Fig. 4). To further elucidate this observation, we introduce the concept of a GR region, which refers to a set of particles that experience the top 1% reduction in inter-particle force magnitudes. A single GR region was first established at Steps 4-5. Locations with high D^2_{\min} values also concentrated towards a single region (right lower part of the sample) and formed a single cluster at the beginning of Stage II (Steps 4-5) (Fig. 4). This single clustered region of elevated D^2_{\min} coincided with the single GR region. In this instance, we therefore conclude that the particle rearrangement under study originated from the weakening of the single GR region.

From Step 6 of this stress drop event, the single GR region no longer existed, likely due to force chain collapse. Figure 4 shows that, from Step 6 to Step 9, the differential force change propagated away from the location where the single GR region had first been established. In addition, the D^2_{\min} distribution shows

that particle rearrangements continued occurring at the location where the single GR region was first established in Steps 6-9 (Fig. 4). Thus, the elimination of the single GR cluster, potentially through force chain collapse, caused both the differential force change propagation and particle rearrangement propagation.

In any contact points other than those in the single GR region, inter-particle force change was almost zero during Steps 4-5 (Fig. 4). Thus, a macroscale stress drop in the normalized shear stress-strain curve appears to occur due to a significant inter-particle force decrease in the GR region and the subsequent structural change in the sample. In Stage III, differential force changes and the propagation of particle rearrangements ended. Figure 5 shows that differential forces and D^2_{\min} were randomly distributed during Stage III.

Figure 7 illustrates the non-affine displacement field during Stages I-III. There was a distinct region of concentrated non-affine displacement at each of Steps 5-6. This region coincided with the single clustered region of high D^2_{\min} , or STZ, in Figure 4. During these steps, the non-affine displacement field exhibited quadrupolar symmetry, consistent with observations made in previous studies for amorphous materials (Hieronymus-Schmidt *et al.*, 2017; Shi *et al.*, 2023).

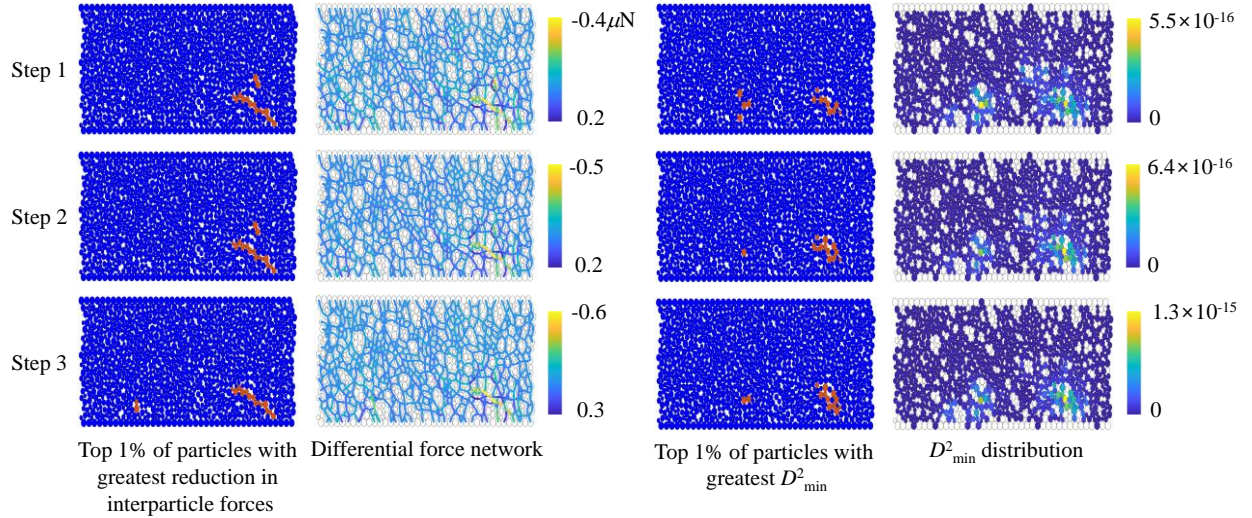


Fig. 3. Top 1% of particles with the greatest reduction in inter-particle force magnitude, differential force network, top 1% of particles with greatest D^2_{\min} , and D^2_{\min} distribution in Stage I.

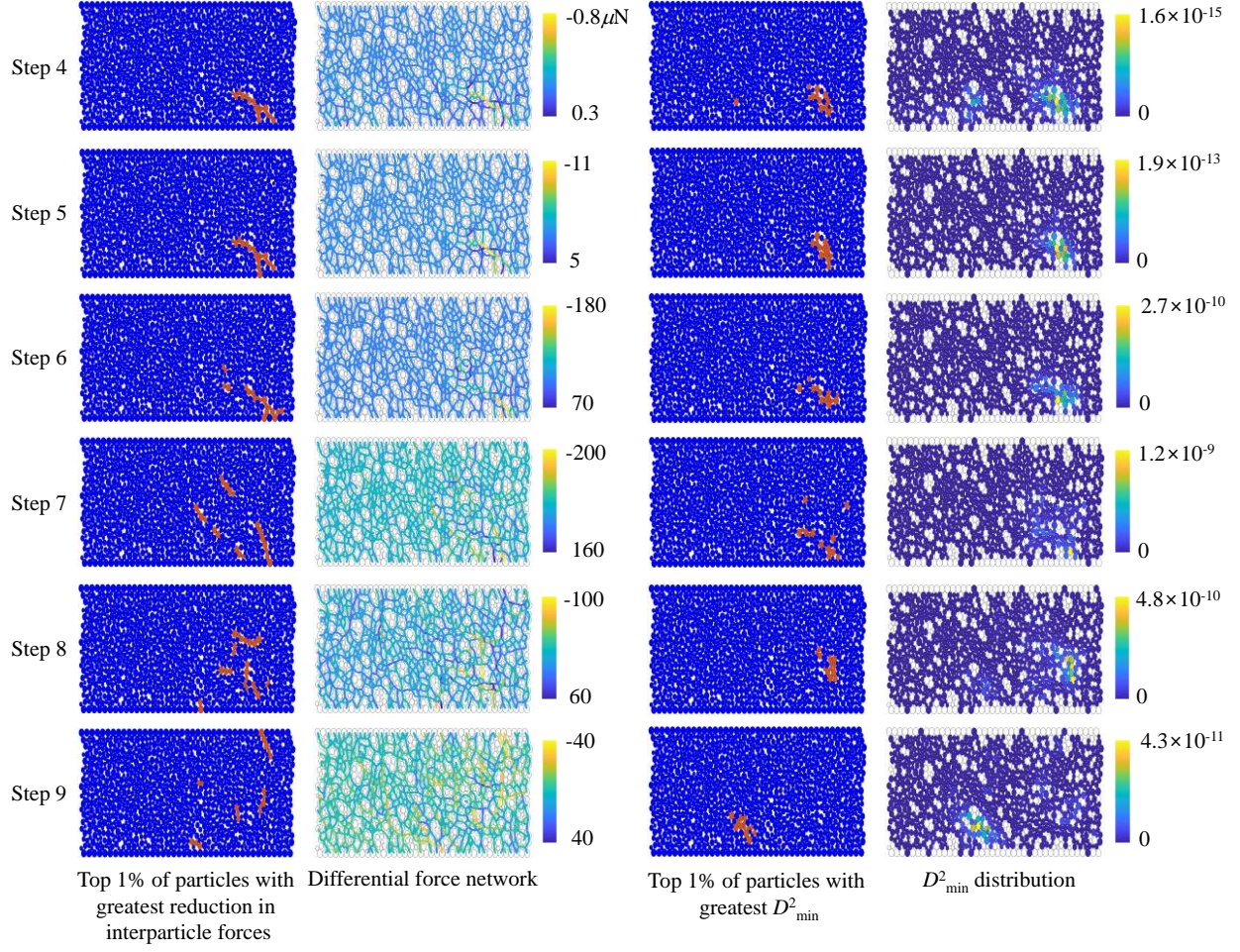


Fig. 4. Top 1% of particles with the greatest reduction in inter-particle force magnitude, differential force network, top 1% of particles with greatest D^2_{\min} , and D^2_{\min} distribution in in Stage II.

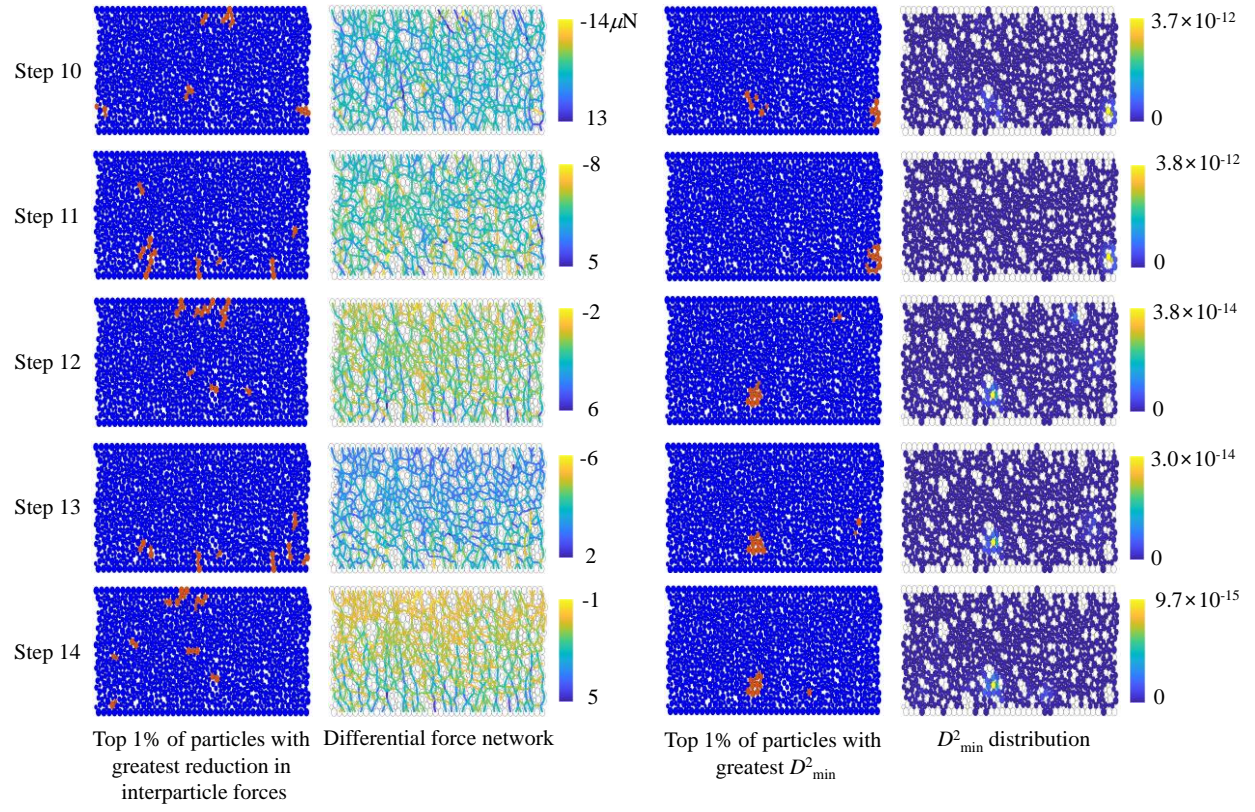


Fig. 5. Top 1% of particles with the greatest reduction in inter-particle force magnitude, differential force network, top 1% of particles with greatest D^2_{\min} , and D^2_{\min} distribution in Stage III.

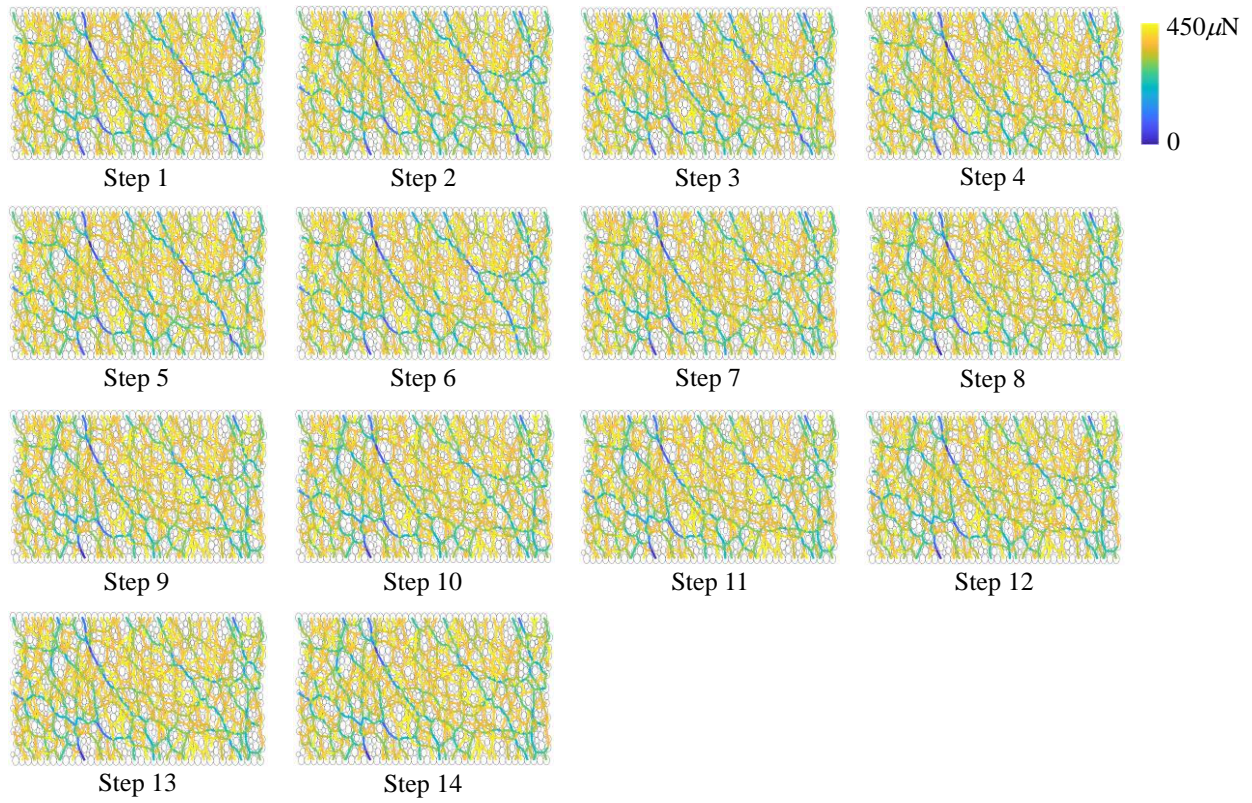


Fig. 6. Force network around the slip event. Lines connecting particle centers are colored by the magnitude of the corresponding inter-particle force.

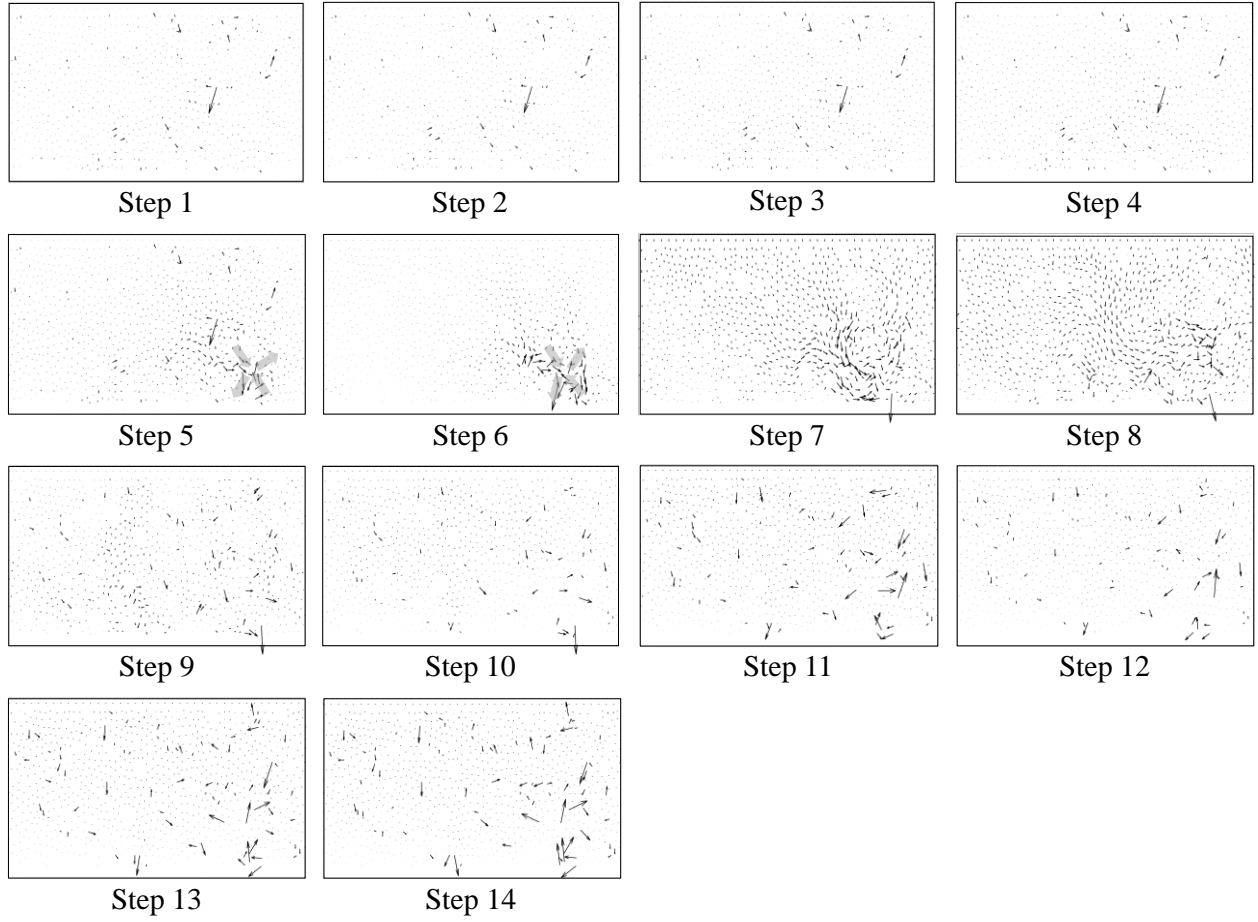


Fig. 7. Non-affine displacement field around the slip event. The arrows represent the non-affine displacement vectors, with the length of each arrow indicating its relative magnitude. Note that the arrow lengths are scaled differently for each step to highlight relative displacements. The gray arrows in Steps 5-6 indicate tension and compression directions.

The Spearman correlation coefficients between the absolute values of the maximum principal stress changes at particles, $|\Delta\sigma_p|$, and D^2_{\min} during the 10.0555 - 10.0575% sample shear strain are given in Figure 8a. This curve shows that the correlation between $|\Delta\sigma_p|$ and D^2_{\min} was high during Steps 4-5, as particle rearrangement was primarily driven by the weakening of the single GR region. However, from Step 6 in Stage II, the correlation between $|\Delta\sigma_p|$ and D^2_{\min} became weak because the single GR region collapsed and the tendency for particle rearrangements propagated outward.

Figure 8b illustrates the greatest D^2_{\min} value, denoted as gD^2_{\min} , and the average of the greatest top 10% D^2_{\min} values, denoted as $g_{10\%}D^2_{\min}$, within the sample across each timestep during the 10.0555 - 10.0575% sample shear strain. Defining a stable structure as one in which particle rearrangement does not occur, the

sample exhibited stability in Stage I marked by low gD_{\min}^2 values. At the onset of Stage II, we observed an increase in gD_{\min}^2 , which signifies the beginning of an instability. Conversely, in Stage III, gD_{\min}^2 gradually decreased, indicating a return toward stability. However, the normalized shear stress-strain curve fluctuated over short time periods in Stage III (Fig. 2b). The $g_{t10\%}D_{\min}^2$ shows the same trend with gD_{\min}^2 during the 10.0555 - 10.0575% sample shear strain, with slightly lower values.

Figure 8c illustrates the number of GR regions during the 10.0555 - 10.0575% sample shear strain. To identify and differentiate these regions, the DBSCAN (Density-Based Spatial Clustering of Applications with Noise) algorithm was employed in MATLAB R2020a. The parameter set for each region included a neighborhood search radius of $r = 5r_p$ and a minimum requirement of 1 neighbor for a point to be considered a core point. Initially, in Stage I, the GR regions were multiple and spatially dispersed (Fig. 3). At the onset of Stage II, they converged into a single region before dispersing once again in Stage III (Figs. 4-5). The number of GR regions increased and decreased in Fig. 8c, reflecting those phenomena.

Figure 8d shows the average and median of the absolute values of the contact angles in the GR regions during the 10.0555 - 10.0575% sample shear strain. The contact angle at a contact point α , θ_α , is defined as an angle (in radians) between the x -axis and an inter-particle force vector. Both the average and median of the absolute values of contact angles in the GR force regions fluctuated significantly from Stage II, indicating no discernible trends once particle rearrangement started to occur.

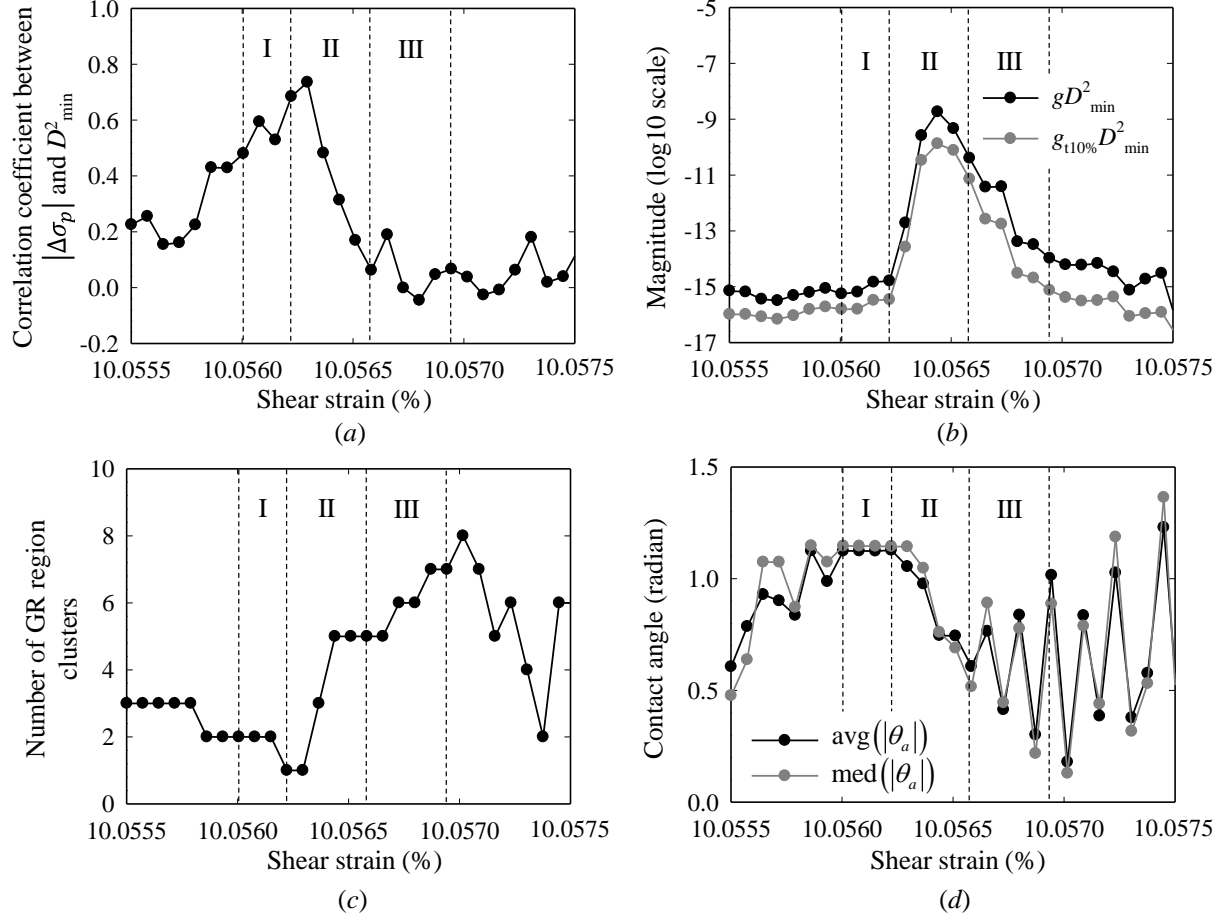


Fig. 8. (a) The Spearman correlation coefficients between the absolute values of maximum principal stress change at particles, $|\Delta\sigma_p|$, and D_{\min}^2 , (b) the greatest D_{\min}^2 and the average of greatest top 10% D_{\min}^2 magnitudes, (c) the number of GR region clusters, and (d) the average and the median of the absolute values of the contact angles in the GR region during 10.0555 to 10.0575% sample shear strain.

3.3. Statistical analysis

In this section, we build upon the initial observations noted for a single stress drop event in Section 3.2 and statistically analyze the results of the entire DEM simulation. Using the data from approximately 130,000 timesteps and 42,000 observed phases (stick and slip events) in the stick-slip regime (shear strain $\geq 2.2\%$), we investigated which microscopic parameters are strongly correlated with the change of normalized shear stress, $\Delta\tau$, across timesteps and phases.

In Section 3.2, we discovered that when a particular stress drop occurred, particles experiencing the greatest reduction in inter-particle forces were spatially clustered and particle rearrangements originated from this region due to the weakening of inter-particle forces. A single particle with the greatest D_{\min}^2 value

in a sample may primarily determine the overall particle rearrangement behavior. Thus, gD_{\min}^2 emerges as a promising parameter that is strongly correlated with $\Delta\tau$ across all instantaneous timesteps. On the other hand, the single particle with the greatest D_{\min}^2 value may induce shear transformations in neighboring zones in various ways, depending on the surrounding structures. Therefore, $g_{t10\%}D_{\min}^2$ may also be a promising parameter that is strongly correlated with $\Delta\tau$ across all instantaneous timesteps. Figure 9a illustrates the absolute values of the Spearman correlation coefficients between $\Delta\tau$ and both gD_{\min}^2 and $g_{t10\%}D_{\min}^2$ across all instantaneous timesteps within the stick-slip regime. We omit correlation coefficient data from all figures in this paper where the P -value exceeds 0.05, ensuring that only statistically significant results are presented. The analysis reveals that $\Delta\tau$ is weakly correlated with both gD_{\min}^2 and $g_{t10\%}D_{\min}^2$ when $\Delta\tau$ decreases significantly ($-10^{-1} < \Delta\tau < -10^{-2}$), and moderately correlated at higher values of $\Delta\tau$ ($-10^{-2} < \Delta\tau < -10^{-3}$). Conversely, when $\Delta\tau$ increases significantly ($10^{-3} < \Delta\tau < 10^{-2}$), the correlation with both parameters is moderate.

Although $\Delta\tau$ shows a weak to moderate correlation with both gD_{\min}^2 and $g_{t10\%}D_{\min}^2$ when it decreases considerably within the range of -10^{-1} to -10^{-3} , Figures 2b and 8b show that $\Delta\tau$ lags behind the increase of gD_{\min}^2 and $g_{t10\%}D_{\min}^2$. Consequently, instead of focusing on the correlation between $\Delta\tau$ and gD_{\min}^2 or between $\Delta\tau$ and $g_{t10\%}D_{\min}^2$ across all instantaneous timesteps, our focus now shifts to assessing the correlation between the cumulative change in $\Delta\tau$ across a phase, $\Delta\tau_p$, defined as the change of normalized shear stress from the start to the end of a phase, and four supplementary parameters. The first supplementary parameter is the peak value of gD_{\min}^2 observed in a sample during an ascending or descending phase (Equation 1). The second examines the peak value of $g_{t10\%}D_{\min}^2$ observed in a sample during either an ascending or descending phase (Equation 2). The third is the sum of the gD_{\min}^2 values within a phase (Equation 3), starting from t_s , the initial timestep when the GR regions are at their minimum, to t_e , the concluding timestep of the ascending or descending phase. The fourth parameter is the sum of the $g_{t10\%}D_{\min}^2$ values within a phase (Equation 4), starting from t_s to t_e . Mathematically, these parameters are given by:

$$mgD_{\min}^2 = \max_{\text{phase}}(gD_{\min}^2) \quad (1)$$

$$mg_{t10\%}D_{\min}^2 = \max_{\text{phase}}(g_{t10\%}D_{\min}^2) \quad (2)$$

$$sgD_{\min}^2 = \sum_{t=t_s}^{t_e} gD_{\min}^2 \quad (3)$$

$$sg_{t10\%}D_{\min}^2 = \sum_{t=t_s}^{t_e} g_{t10\%}D_{\min}^2 \quad (4)$$

Figure 9b illustrates the absolute values of the Spearman correlation coefficients between $\Delta\tau_p$ and

mgD_{\min}^2 , $\Delta\tau_p$ and $mg_{t10\%}D_{\min}^2$, $\Delta\tau_p$ and sgD_{\min}^2 , and $\Delta\tau_p$ and $sg_{t10\%}D_{\min}^2$, for all phases in the stick-slip regime (shear strain $\geq 2.2\%$). For $-10^{-1} < \Delta\tau_p < -10^{-3}$, the correlations between $\Delta\tau_p$ and all four metrics across the phases show stronger associations compared to those of $\Delta\tau$ with gD_{\min}^2 and $g_{t10\%}D_{\min}^2$ across all instantaneous timesteps ($-10^{-1} < \Delta\tau < -10^{-3}$), as depicted in Figure 9a-b. This greater correlation observed for all phases, rather than across all individual timesteps, suggests that analyzing microscopic dynamics throughout the duration of a phase provides a better link to the macroscale responses of granular materials. The results show that the correlation curves for $\Delta\tau_p$ with sgD_{\min}^2 and $\Delta\tau_p$ with mgD_{\min}^2 exhibit similar trends, both indicating a moderate to strong correlation within the range of $-10^{-1} < \Delta\tau_p < -10^{-3}$. This also implies that it is sufficient to consider only particle dynamics at some points within the phase of the most pronounced non-affine motion, rather than examining the dynamics throughout the entire phase. On the other hand, the correlation between $\Delta\tau_p$ and $mg_{t10\%}D_{\min}^2$ as well as $\Delta\tau_p$ and $sg_{t10\%}D_{\min}^2$ demonstrates a slightly stronger correlation than the other metrics in the same $\Delta\tau_p$ range. This suggests that the variability in the D_{\min}^2 values of the particles surrounding the particle with gD_{\min}^2 affects $\Delta\tau_p$ to at least a small extent.

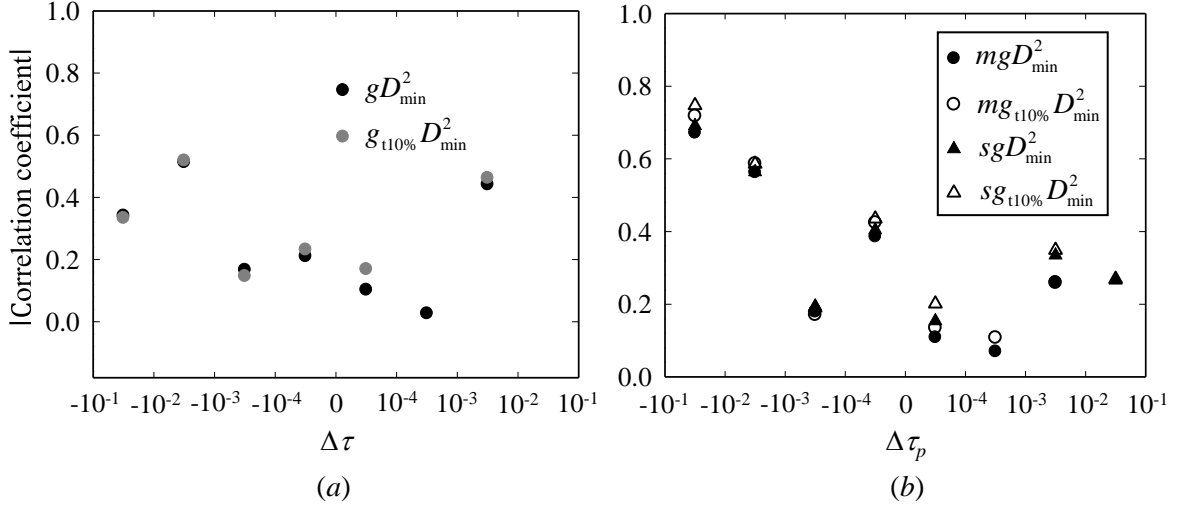


Fig. 9. (a) Graphs of the absolute values of the Spearman correlation coefficients between $\Delta\tau$ and gD_{\min}^2 and between $\Delta\tau$ and $g_{t10\%}D_{\min}^2$ across all instantaneous timesteps in the stick-slip regime, and (b) Graphs of the absolute values of the Spearman correlation coefficients between $\Delta\tau_p$ and mgD_{\min}^2 , $\Delta\tau_p$ and $mg_{t10\%}D_{\min}^2$, $\Delta\tau_p$ and sgD_{\min}^2 , and $\Delta\tau_p$ and $sg_{t10\%}D_{\min}^2$, for all phases in the stick-slip regime.

Figure 10a-b show the absolute values of the Spearman correlation coefficients graphs for $\Delta\tau_p - mgD_{\min}^2$, $\Delta\tau_p - mg_{t10\%}D_{\min}^2$, $\Delta\tau_p - sgD_{\min}^2$, and $\Delta\tau_p - sg_{t10\%}D_{\min}^2$ in long (l) phases where $t_p > 3\Delta\gamma$ (here, t_p denotes the duration of the phase) and short (s) phases where $t_p \leq 3\Delta\gamma$, respectively, in the stick-slip regime. It is observed that τ can exhibit fluctuations having short phases, as exemplified by Stage III illustrated in Figure 2b, when the structure is unstable. Given their distinct behaviors as compared to long phases, we examine both long and short phases separately.

The results indicate that the correlations for $\Delta\tau_p - mgD_{\min}^2$, $\Delta\tau_p - mg_{t10\%}D_{\min}^2$, $\Delta\tau_p - sgD_{\min}^2$, and $\Delta\tau_p - sg_{t10\%}D_{\min}^2$ in long phases not only follow the same trend as those observed in all phases but are also stronger, particularly when $-10^{-1} < \Delta\tau_p < -10^{-4}$ (Fig. 9b). Among correlated variables, $\Delta\tau_p - mg_{t10\%}D_{\min}^2$ and $\Delta\tau_p - sg_{t10\%}D_{\min}^2$ exhibit a stronger correlation than $\Delta\tau_p - mgD_{\min}^2$ and $\Delta\tau_p - sgD_{\min}^2$, respectively, in long phases during the slip events ($\Delta\tau_p < 0$). This indicates that the variability in the D_{\min}^2 values of the particles surrounding the particle with gD_{\min}^2 influences $\Delta\tau$ to some extent in long phases during the slip events. During the slip events ($\Delta\tau_p < 0$), the correlations between $\Delta\tau_p$ and $sg_{t10\%}D_{\min}^2$ are stronger than those between $\Delta\tau_p$ and $mg_{t10\%}D_{\min}^2$ in long phases. This indicates that the phenomenon is history-dependent, as $sg_{t10\%}D_{\min}^2$ reflects the overall behavior of particle rearrangements during a slip event. In addition, during the slip events ($\Delta\tau_p < 0$), the correlations between $\Delta\tau_p$ and both $mg_{t10\%}D_{\min}^2$ and $sg_{t10\%}D_{\min}^2$ for long phases are strong for a significant decrease in $\Delta\tau_p$ ($\Delta\tau_p < -10^{-2}$) and mostly moderate for a small decrease in $\Delta\tau_p$ ($-10^{-2} < \Delta\tau_p < 0$). The correlations for $\Delta\tau_p - mgD_{\min}^2$, $\Delta\tau_p - mg_{t10\%}D_{\min}^2$, $\Delta\tau_p - sgD_{\min}^2$, and $\Delta\tau_p - sg_{t10\%}D_{\min}^2$ in short phases are significantly weaker than those in long phases when $-10^{-1} < \Delta\tau_p < -10^{-4}$.

Figure 10c displays the graphs of the absolute values of the Spearman correlation coefficients of $\Delta\tau_p$ with t_p for both long and short phases in the stick-slip regime. The results show that $\Delta\tau_p - t_p$ is moderately correlated for large $\Delta\tau_p$ values ($\Delta\tau_p > 10^{-4}$) in the long stick events. Unlike in the slip events, the structure of a sample in the stick events is stable, exhibiting small gD_{\min}^2 values for long phases, and thus τ_p increases slowly as t_p increases. On the other hand, particle rearrangement is dominant for the long slip events. Thus, $\Delta\tau_p - t_p$ is weakly correlated for the slip events ($\Delta\tau_p < 0$) in long phases. In short phases, $\Delta\tau_p - t_p$ shows a weak correlation.

Figure 11a-b shows the graphs of the absolute values of the Spearman correlation coefficients of $\Delta\tau_p$ with both the average and median of the absolute contact angles in GR regions across various ranges of $mg_{t10\%}D_{\min}^2$ and $sg_{t10\%}D_{\min}^2$, respectively, during long phases in the stick-slip regime. These values are calculated at the final timestep of each phase when the number of GR regions is at its minimum. The results indicate that the correlations between $\Delta\tau_p$ and both the average and median of the absolute contact angles

in GR regions across various ranges of $mg_{t10\%}D_{\min}^2$ and $sg_{t10\%}D_{\min}^2$ during long phases are either weak or not statistically significant (P -value > 0.05). Consequently, it can be inferred that the contact structure of the single GR region does not significantly influence $\Delta\tau_p$. This observation is attributed to the substantial fluctuations in the mean and median of the contact angles following the collapse of the single GR region, as illustrated in Fig. 8d.

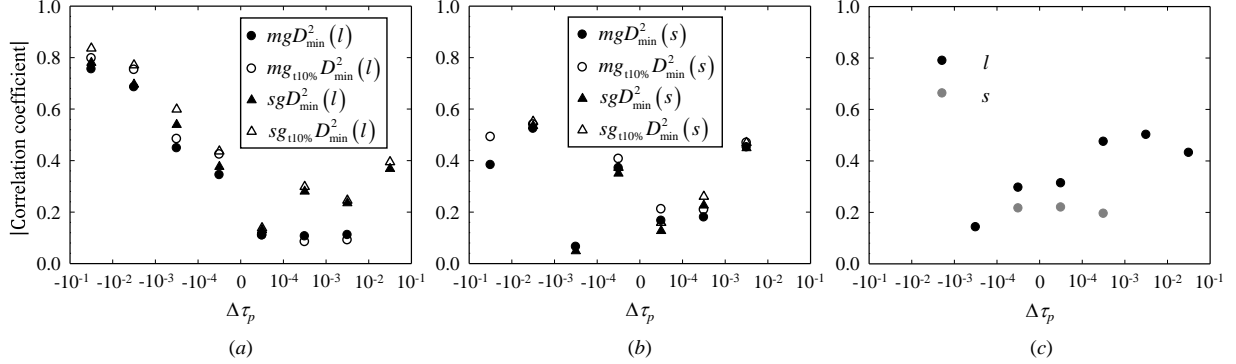


Fig. 10. Graphs of the absolute values of the Spearman correlation coefficients for $\Delta\tau_p - mgD_{\min}^2$, $\Delta\tau_p - mg_{t10\%}D_{\min}^2$, $\Delta\tau_p - sgD_{\min}^2$, and $\Delta\tau_p - sg_{t10\%}D_{\min}^2$ for (a) long, l , ($> 3\Delta\gamma$) phases and (b) short, s , ($\leq 3\Delta\gamma$) phases in the stick-slip regime; and (c) Graphs of Spearman correlation coefficient for $\Delta\tau_p - t_p$ for long, l , ($> 3\Delta\gamma$) and short, s , ($\leq 3\Delta\gamma$) phases in the stick-slip regime.

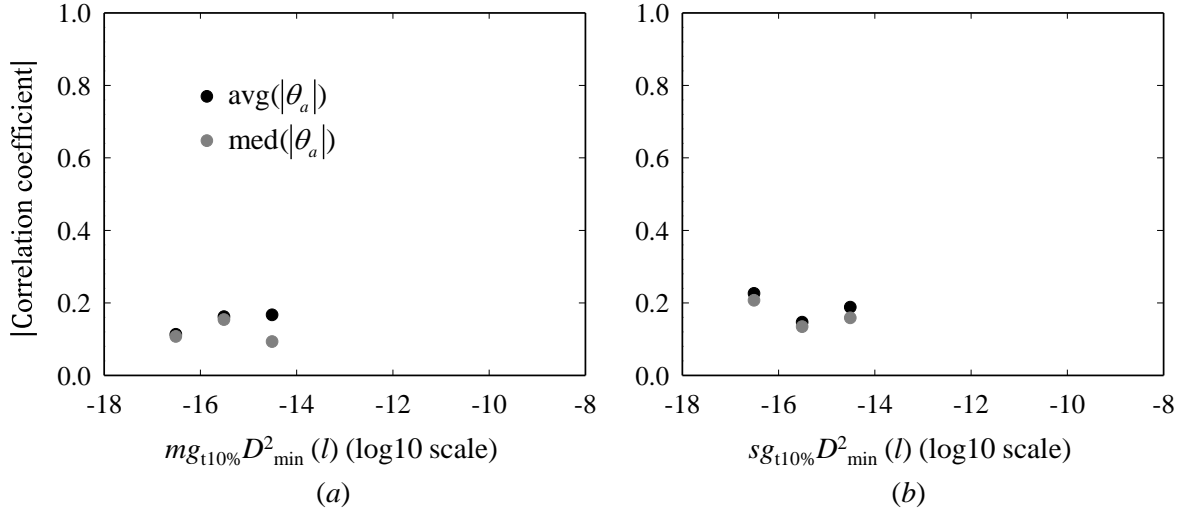


Fig. 11. Graphs of the absolute values of the Spearman correlation coefficients of $\Delta\tau_p$ with both the average and median of the absolute contact angles in GR regions across various ranges of (a) $mg_{t10\%}D_{\min}^2$ and (b) $sg_{t10\%}D_{\min}^2$ during long phases in the stick-slip regime. Here, these values are calculated at the final timestep of each phase, when the number of GR regions is at its minimum.

4. Sliding friction coefficients

To study the effect of sliding friction coefficients on stick-slip behavior, we conducted additional DEM simulations with μ_s values including 0.1, 0.3, and 0.5, to complement the simulation with a μ_s value of 0.7 described in Sections 2 and 3. The boundary conditions, material properties, and contact properties otherwise remained the same as those used in the DEM simulation described in Section 2.

Figure 12 displays the normalized shear stress-strain curves for various sliding friction coefficients. In the stick-slip regime (shear strain $\geq 2.2\%$), curves for $\mu_s = 0.1, 0.3, 0.5$, and 0.7 were similar. During the slip events, the microscopic dynamics and force network for $\mu_s = 0.1, 0.3$, and 0.5 followed a similar trend to those observed for $\mu_s = 0.7$, which are explained in Section 3.2.

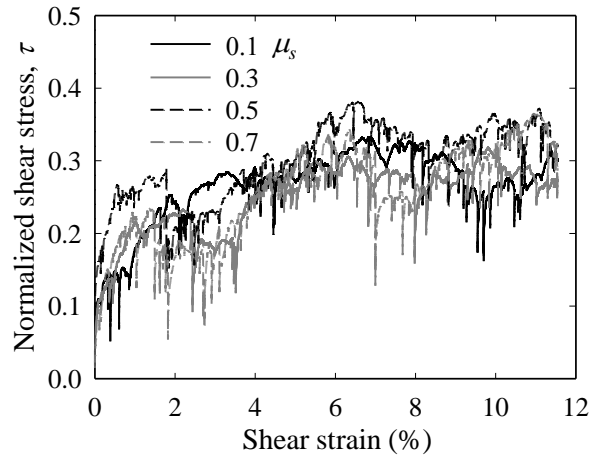


Fig. 12. Normalized shear stress-strain curve from discrete element method simulation for various sliding friction coefficients.

Employing a dataset that includes approximately 130,000 timesteps for each of four simulations with sliding friction coefficients ($\mu_s = 0.1, 0.3, 0.5$, and 0.7), we observed approximately 18,000 phases for $\mu_s = 0.1$, 46,000 for $\mu_s = 0.3$, 52,000 for $\mu_s = 0.5$, and 42,000 for $\mu_s = 0.7$ within the stick-slip regime. We examined the correlations between various parameters and $\Delta\tau$ across these timesteps and phases. Figure 13 illustrates the absolute values of the Spearman correlation coefficients between kinematic measures and $\Delta\tau$ or $\Delta\tau_p$ for various sliding friction coefficients, with each value of μ_s represented by different symbols, in the stick-slip regime. Specifically: (a) shows the correlation coefficient between $\Delta\tau$ and $g_{t10\%}D_{\min}^2$ across all instantaneous timesteps, (b) depicts the correlation coefficient between $\Delta\tau_p$ and $mg_{t10\%}D_{\min}^2$ for all phases, (c) displays the correlation coefficient between $\Delta\tau_p$ and $mg_{t10\%}D_{\min}^2$ for long (l) phases, where t_p is greater than $3\Delta\gamma$, (d) shows the correlation coefficient between $\Delta\tau_p$ and $mg_{t10\%}D_{\min}^2$ for short (s) phases, where t_p is

less than or equal to $3\Delta\gamma$, (e) displays the correlation coefficient between $\Delta\tau_p$ and mgD_{\min}^2 for long (l) phases, where t_p is greater than $3\Delta\gamma$, (f) depicts the correlation coefficient between $\Delta\tau_p$ and $sg_{t10\%}D_{\min}^2$ for all phases, (g) displays the correlation coefficient between $\Delta\tau_p$ and $sg_{t10\%}D_{\min}^2$ for long (l) phases, where t_p is greater than $3\Delta\gamma$, (h) shows the correlation coefficient between $\Delta\tau_p$ and $sg_{t10\%}D_{\min}^2$ for short (s) phases, where t_p is less than or equal to $3\Delta\gamma$, (i) displays the correlation coefficient between $\Delta\tau_p$ and sgD_{\min}^2 for long (l) phases, where t_p is greater than $3\Delta\gamma$, and (j) shows the correlation coefficient between $\Delta\tau_p$ and t_p for long (l) phases, where t_p is greater than $3\Delta\gamma$.

Figure 13a-i demonstrates consistent trends in the correlations between $\Delta\tau$ and $g_{t10\%}D_{\min}^2$ across all instantaneous timesteps and between $\Delta\tau_p$ and both $mg_{t10\%}D_{\min}^2$ and $sg_{t10\%}D_{\min}^2$ for all phases, long phases, and short phases, for all μ_s values. Figure 13a-b and f shows that the correlations between $\Delta\tau_p$ and both $mg_{t10\%}D_{\min}^2$ and $sg_{t10\%}D_{\min}^2$ across all phases during the slip events ($\Delta\tau_p < 0$) mostly have stronger associations compared to those of $\Delta\tau$ with $g_{t10\%}D_{\min}^2$ across all instantaneous timesteps for $-10^{-1} < \Delta\tau < -10^{-3}$ for all μ_s values. These stronger correlations observed for all phases, as opposed to individual timesteps, indicate that examining the microscopic dynamics over the entire duration of a phase provides a better understanding of the macroscale responses of granular materials. Figure 13b-c and f-g shows that $\Delta\tau_p - mg_{t10\%}D_{\min}^2$ and $\Delta\tau_p - sg_{t10\%}D_{\min}^2$ in long phases not only follow the same trend as those observed in all phases but are also mostly more highly correlated, particularly during the slip events ($\Delta\tau_p < 0$) across all μ_s values. The correlations between $\Delta\tau_p$ and both $mg_{t10\%}D_{\min}^2$ and $sg_{t10\%}D_{\min}^2$ for long phases are strong for a significant decrease in $\Delta\tau_p$ ($\Delta\tau_p < -10^{-2}$) and mostly moderate for a small decrease in $\Delta\tau_p$ ($10^{-2} < \Delta\tau_p < 0$) across all μ_s values. On the other hand, Figure 13d and h shows that $\Delta\tau_p - mg_{t10\%}D_{\min}^2$ and $\Delta\tau_p - sg_{t10\%}D_{\min}^2$ in short phases are not strongly correlated for all $\Delta\tau_p$ regimes across all μ_s values. This is because τ can show fluctuations during short phases, as depicted in Stage III shown in Figure 2b, when the structure is unstable. Figure 13c, e, g, and i shows that the correlations between $\Delta\tau_p$ and both $mg_{t10\%}D_{\min}^2$ and $sg_{t10\%}D_{\min}^2$ for long phases are consistently stronger than those between $\Delta\tau_p$ and both mgD_{\min}^2 and sgD_{\min}^2 during the slip events ($\Delta\tau_p < 0$), indicating that variability in D_{\min}^2 values of particles surrounding the one with the greatest D_{\min}^2 value influences $\Delta\tau_p$ to some extent during the slip events for all μ_s values. Figure 13c and g shows that during the slip events ($\Delta\tau_p < 0$), the correlations between $\Delta\tau_p$ and $sg_{t10\%}D_{\min}^2$ are almost equal to or stronger than those between $\Delta\tau_p$ and $mg_{t10\%}D_{\min}^2$ in long phases for different μ_s values. This suggests that the phenomenon is dependent on its history for all μ_s values, as $sg_{t10\%}D_{\min}^2$ captures the overall behavior of particle rearrangements throughout a slip event. Figure 13j illustrates varying trends in the correlation between $\Delta\tau_p$ and t_p for long phases for different μ_s values. Notably, in certain stick phases where $\Delta\tau_p$

significantly increases ($10^{-3} < \Delta \tau_p < 10^{-1}$), moderate correlations between $\Delta \tau_p$ and t_p are observed at $\mu_s = 0.5$ and 0.7. In contrast, at lower μ_s values (0.1 and 0.3), these correlations are weak or have high P -values (> 0.05), possibly due to increased particle movement during stick phases at lower sliding friction levels.

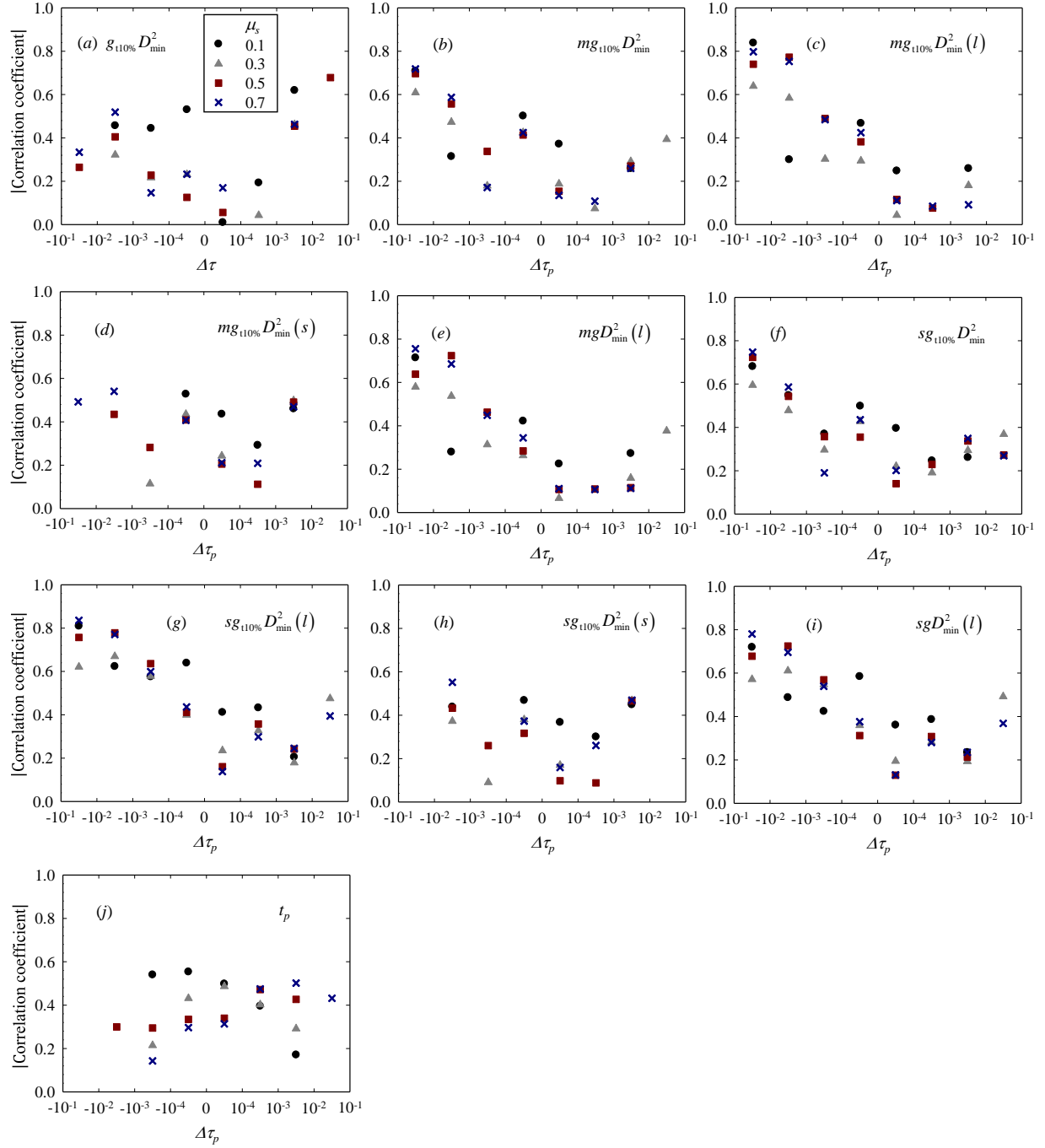


Fig. 13. Graphs of the absolute values of the Spearman correlation coefficients between kinematic measures and $\Delta\tau$ or $\Delta\tau_p$ for various sliding friction coefficients, with each value of μ_s represented by different symbols, in the stick-slip regime; (a) $\Delta\tau - g_{t10\%}D_{\min}^2$ across all instantaneous timesteps, (b) $\Delta\tau_p - mg_{t10\%}D_{\min}^2$ for all phases, (c) $\Delta\tau_p - mg_{t10\%}D_{\min}^2$ for long, l , ($> 3\Delta\gamma$) phases, (d) $\Delta\tau_p - mg_{t10\%}D_{\min}^2$ for short, s , ($\leq 3\Delta\gamma$) phases, (e) $\Delta\tau_p - mgD_{\min}^2$ for long, l , ($> 3\Delta\gamma$) phases, (f) $\Delta\tau_p - sg_{t10\%}D_{\min}^2$ for all phases, (g) $\Delta\tau_p - sg_{t10\%}D_{\min}^2$ for long, l , ($> 3\Delta\gamma$) phases, (h) $\Delta\tau_p - sg_{t10\%}D_{\min}^2$ for short, s , ($\leq 3\Delta\gamma$) phases, (i) $\Delta\tau_p - sgD_{\min}^2$ for long, l , ($> 3\Delta\gamma$) phases, and (j) $\Delta\tau_p - t_p$ for long, l , ($> 3\Delta\gamma$) phases.

5. Larger samples

To investigate the effect of the number of particles on microscopic dynamics, force network fluctuations, and the statistical response during stick-slip behavior, we conducted additional DEM simulations using a larger number of particles. We selected a uniform distribution of particle sizes ranging from 0.2 to 0.4 μm for the particle radius. The total number of particles used was about 5,000. Except for particle sizes, the boundary conditions, material properties, and contact properties were consistent with those used in the DEM model described in Section 2. In particular, for the sliding friction coefficients, μ_s , and rolling friction coefficients, μ_r , values of 0.7 and 0.01 were used, respectively. The macroscale shear strain interval at which simulation data were output for analysis, $\Delta\gamma$, was 1.8×10^{-6} .

The normalized shear stress-strain curve for both simulations with a small and large number of particles is presented in Figure 14a. This figure shows that the average value of the normalized shear stress in the steady-state regime (shear strain $\geq 5.4\%$) for a large number of particles is similar to the average value of the normalized shear stress at the stick-slip regime (shear strain $\geq 2.2\%$) for a smaller number of particles. In the normalized shear stress-strain curve depicted in Fig. 14a, the steady-state regime is identified as the region where the shear strain exceeds 5.4%. This designation is based on the observation that, beyond this point, the normalized shear stress exhibits a relatively stable and consistent pattern compared to the initial deformation before 5.4% shear strain. The simulation with a larger number of particles exhibits smaller magnitudes of normalized shear stress fluctuations compared to those with a small number of particles. Appendix C provides the normalized shear stress-strain curves for various sliding friction coefficients in simulations with a larger number of particles (see Fig. 24).

During the shearing process of the simulation with a larger number of particles, we observed a total of approximately 26,000 phases in the steady-state regime, comprising both stick (ascending) and slip (descending) events in the normalized shear stress-strain curve. Here, we first focused on the region around the largest stress drop observed in the steady-state regime, specifically between 9.380% to 9.384% shear strain as depicted in Fig. 14b. This region around the slip event is delineated into three distinct stages: the pre-stress drop stage (Stage I), the stress drop stage (Stage II), and the post-stress drop stage (Stage III). Here, in Stage II, there were two stress drops. The largest stress drop in the steady-state regime corresponds to the first drop. Right after the first stress drop, we observed one more stress drop (second drop). Figures 15-18 show the top 1% of particles with the greatest reduction in inter-particle force magnitude, differential force network, the top 1% of particles with the greatest D^2_{\min} , and D^2_{\min} distribution in Stages I-III during 9.380 - 9.384% shear strain in Figure 14b. Rattler particles are again excluded from the computation of D^2_{\min} . The colorless disks in the distribution of D^2_{\min} graph in Figures 15-18 are the rattler particles. Figure

19 shows the force network in Stages I-III.

As observed in the simulation with fewer particles (Section 3.2, see Figs. 3-6), the simulation with a larger number of particles also exhibited the same trends in microscopic dynamics and force network fluctuations around the major stress drop region, except that it has two stress drops in Stage II. In this simulation, the initial random distribution of the differential force and D^2_{\min} (Fig. 15) rapidly consolidated into a single cluster in the lower left part of the sample by Step 4 (Fig. 16), indicating the formation of a single clustered GR region and the beginning of the first stress drop. This clustering process, similar to what was observed with fewer particles, highlights the reproducibility of such phenomena across samples of different sizes. From Step 5, the single clustered GR region collapsed, with differential force changes spreading from the location where the single GR region had been established (Fig. 16). This continued rearrangement near this clustered region showed a significant structural change, and it influenced the macroscopic stress response. Notably, outside this clustered region, changes in inter-particle forces remained minimal during these steps (Fig. 16), pointing to a focused area of activity that led to a significant stress drop in the normalized macroscopic shear stress-strain curve. By Step 10, the distribution of the differential force and D^2_{\min} (Fig. 17) rapidly consolidated into a single cluster again in the lower right part of the sample, indicating the formation of another single clustered GR region and the start of the second stress drop. From Step 11, this GR region collapsed, with differential force changes spreading from its location (Fig. 17). By Stage III, the spread of differential force changes from the collapse of the GR region subsided, and both differential force and D^2_{\min} appeared randomly distributed once more in Stage III (Fig. 18).

Figure 20 displays the non-affine displacement field observed in a simulation with a large number of particles throughout Stages I-III. A distinct region of concentrated non-affine displacement, or an STZ, was observed at Steps 5-6, as shown in Figure 17 at the beginning of the first stress drop. During these steps, the non-affine displacement field exhibited quadrupolar symmetry, consistent with previous observations in amorphous materials (Hieronymus-Schmidt *et al.*, 2017; Shi *et al.*, 2023). Similarly, at Steps 10-11, a distinct STZ was observed, as shown in Figure 18 at the beginning of the second stress drop. During these steps, the non-affine displacement field exhibited a vortex shape, also consistent with previous observations in amorphous materials (Shi *et al.*, 2023).

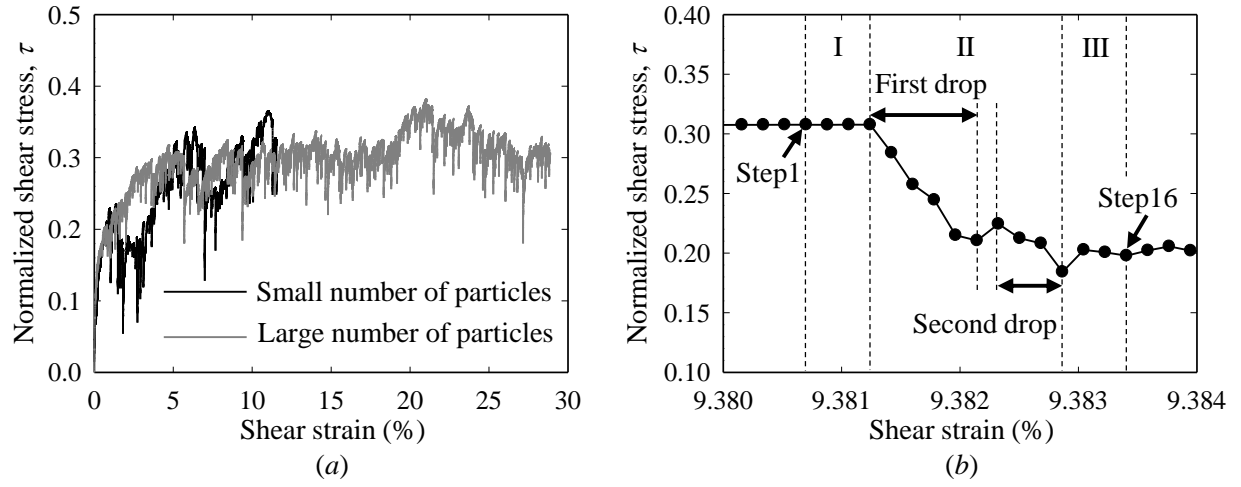


Fig. 14. (a) Normalized shear stress-strain curve from discrete element method simulation for a small and a large number of particles. (b) Normalized shear stress-strain curve around a slip event during 9.380% to 9.384% shear strain for a simulation with a large number of particles; the region around the slip event is delineated into three distinct stages: the pre-stress drop stage (Stage I), the stress drop stage (Stage II), and the post-stress drop stage (Stage III). The first and second stress drops are indicated.

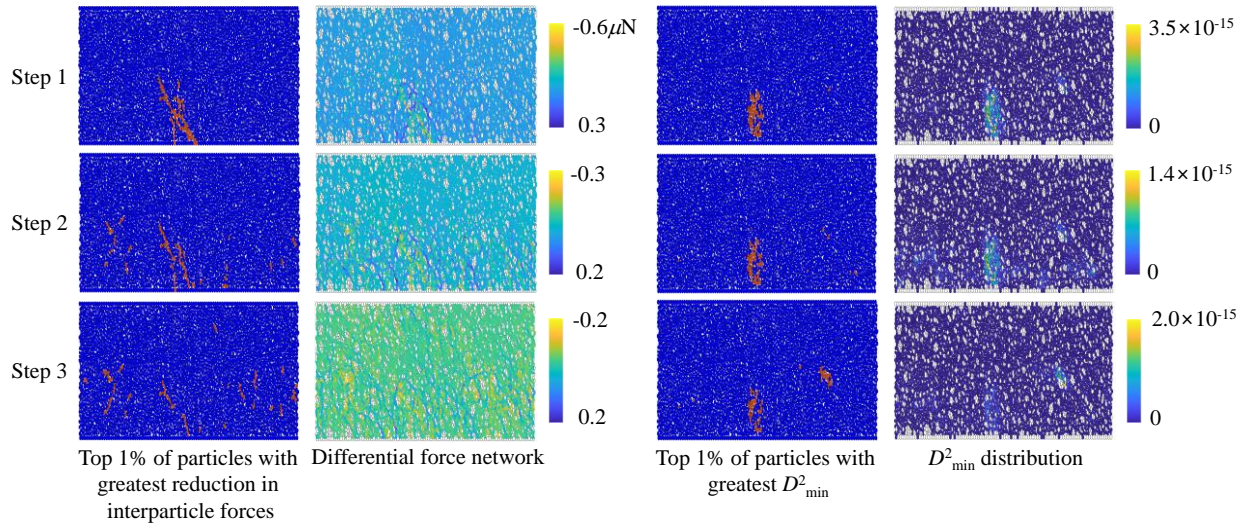


Fig. 15. Top 1% of particles with the greatest reduction in inter-particle forces magnitude, differential force network, top 1% of particles with greatest D^2_{\min} , and D^2_{\min} distribution in Stage I for the simulation with a large number of particles.

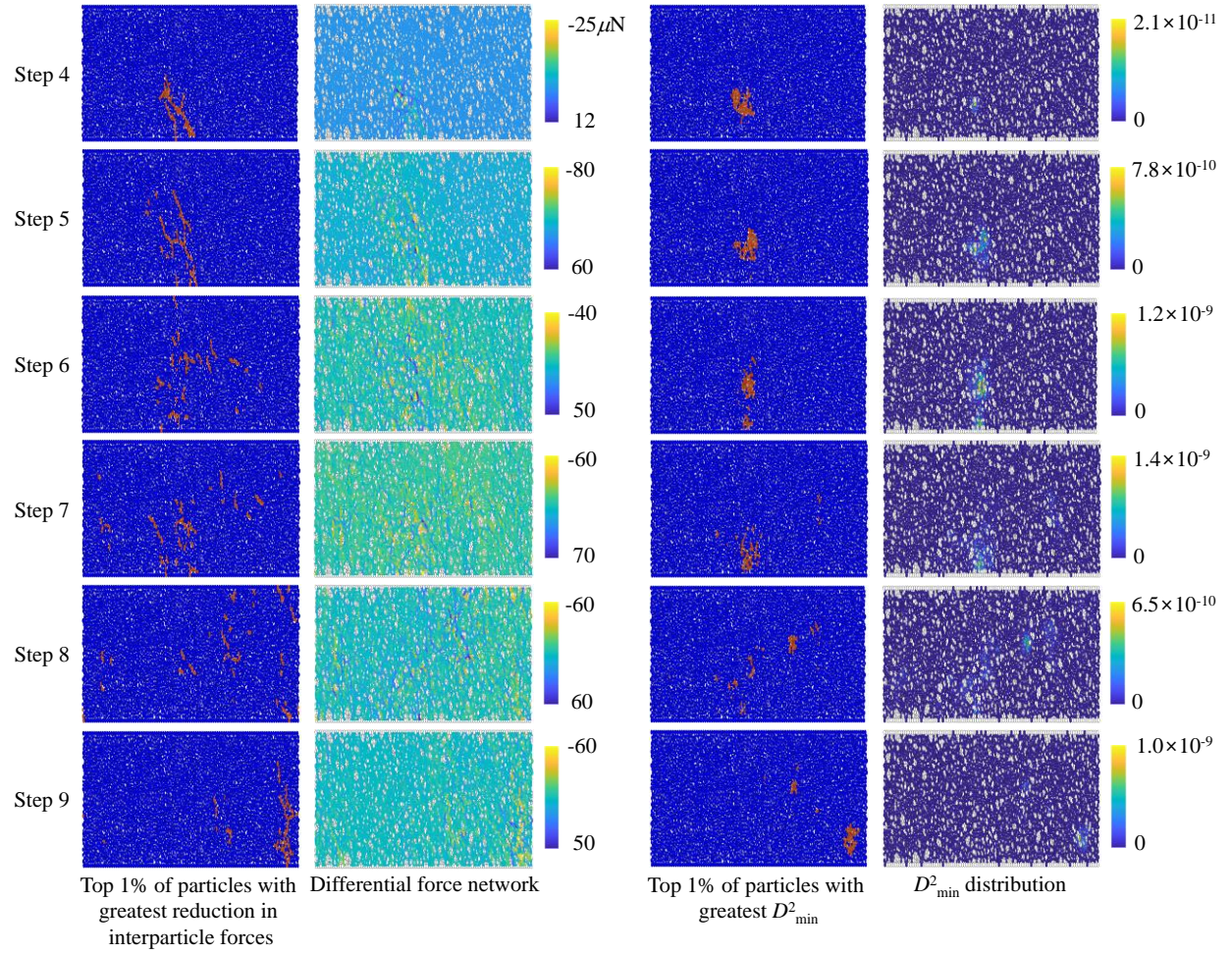


Fig. 16. Top 1% of particles with the greatest reduction in inter-particle forces magnitude, differential force network, top 1% of particles with greatest D^2_{\min} , and D^2_{\min} distribution in Stage II during the first stress drop for the simulation with a large number of particles.

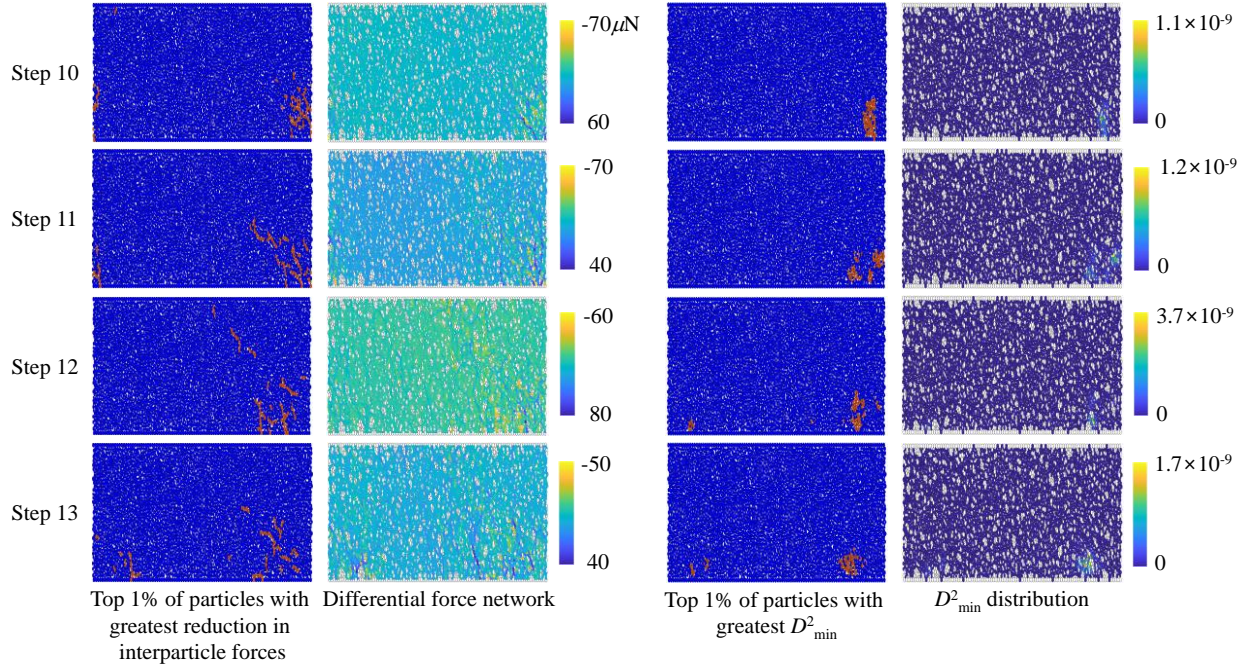


Fig. 17. Top 1% of particles with the greatest reduction in inter-particle forces magnitude, differential force network, top 1% of particles with greatest D^2_{\min} , and D^2_{\min} distribution in Stage II during the second stress drop for the simulation with a large number of particles.

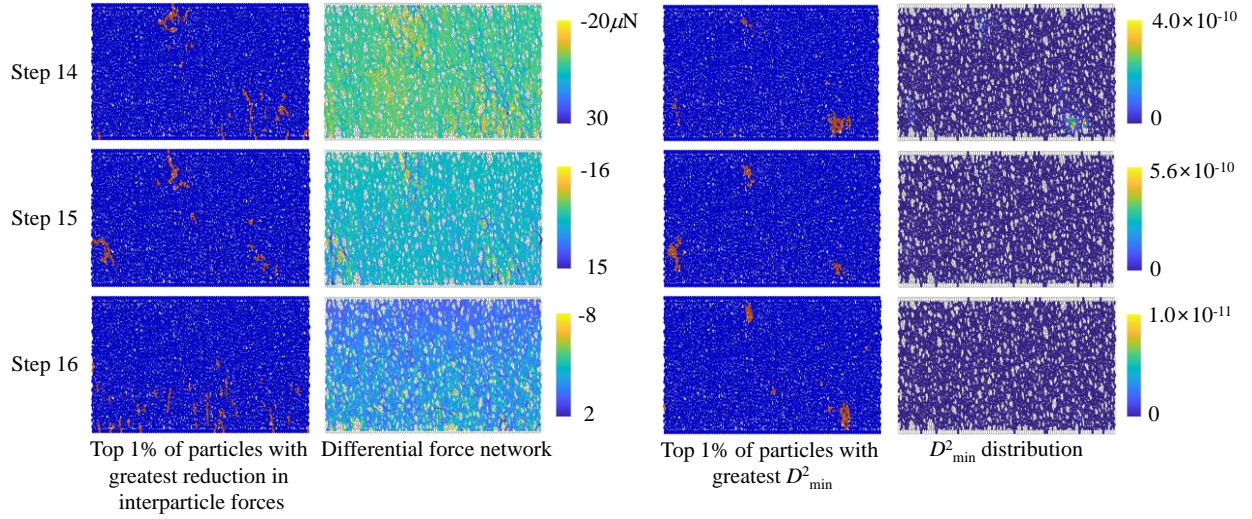


Fig. 18. Top 1% of particles with the greatest reduction in inter-particle forces magnitude, differential force network, top 1% of particles with greatest D^2_{\min} , and D^2_{\min} distribution in Stage III for the simulation with a large number of particles.

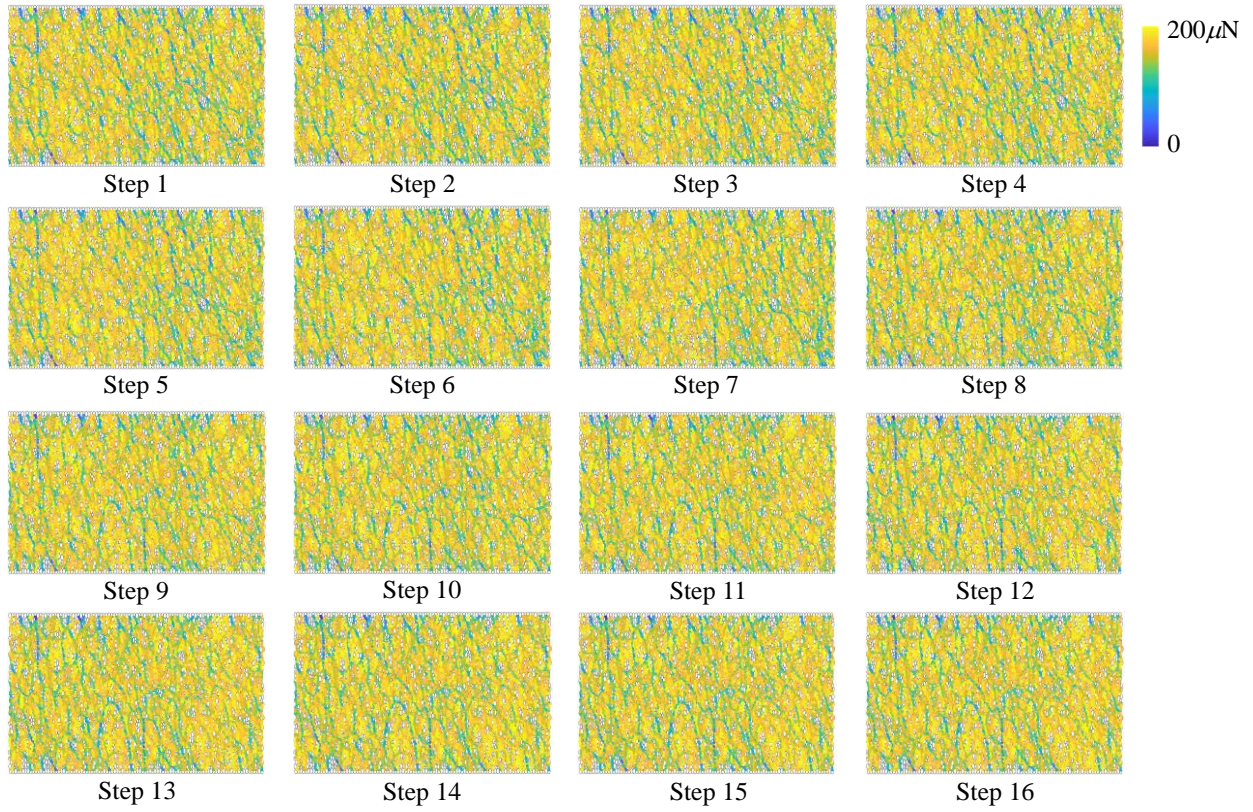


Fig. 19. Force network around the slip event for the simulation with a large number of particles. Lines connecting particle centers are colored by the magnitude of the corresponding inter-particle force.

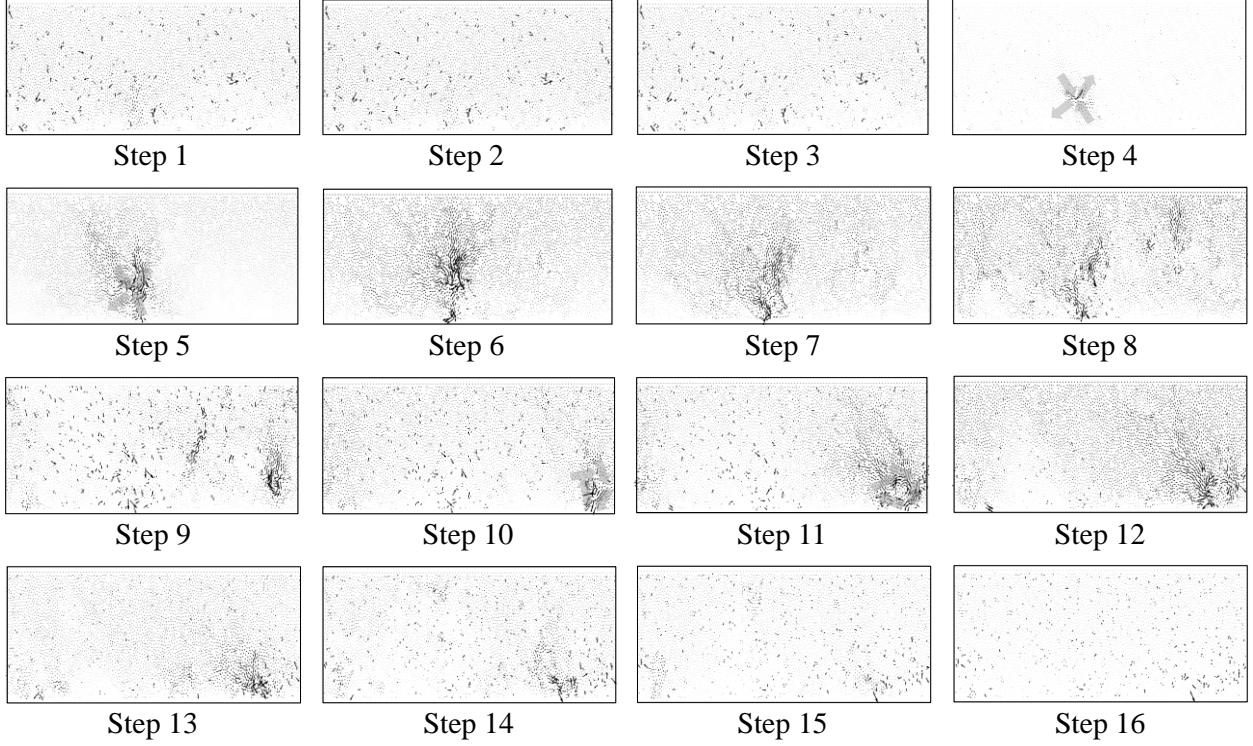


Fig. 20. Non-affine displacement field around the slip event for the simulation with a large number of particles. The arrows represent the non-affine displacement vectors, with the length of each arrow indicating its relative magnitude. Note that the arrow lengths are scaled differently for each step to highlight relative displacements. The gray arrows in Steps 4-5 indicate the directions of tension and compression, and the gray arrows in Steps 10-11 indicate vortex-like flow.

Figure 21 shows (a) the Spearman correlation coefficient between $|\Delta\sigma_p|$ and D_{\min}^2 , (b) the greatest D_{\min}^2 and the average of the greatest top 10% D_{\min}^2 , (c) the number of GR regions, and (d) the average and median contact angles in GR regions during the 9.380 – 9.384% sample shear strain for the simulation with a large number of particles. These correlations and variables follow the same trends as those from the simulation with a smaller number of particles (Fig. 8). Figures 8a and 21a show that, in both simulations, the Spearman correlation coefficients between $|\Delta\sigma_p|$ and D_{\min}^2 are relatively high at the beginning of the stress drops in Stage II because particle rearrangement was caused by the weakening of the clustered GR region. Figures 8b and 21b show that both gD_{\min}^2 and $g_{t10\%}D_{\min}^2$ increased in Stage II and decreased in Stage III in both simulations with a smaller and larger number of particles. We also note that the maximum values of gD_{\min}^2 and $g_{t10\%}D_{\min}^2$ in both simulations during Stage II were almost the same. Figures 8c and 21c illustrate that the number of GR force chain clusters in both simulations drop dramatically at the beginning of the stress

drops in Stage II. Figures 8d and 21d show that the average and the median of the absolute values of the contact angles in the GR region fluctuated significantly from Stage II in both simulations.

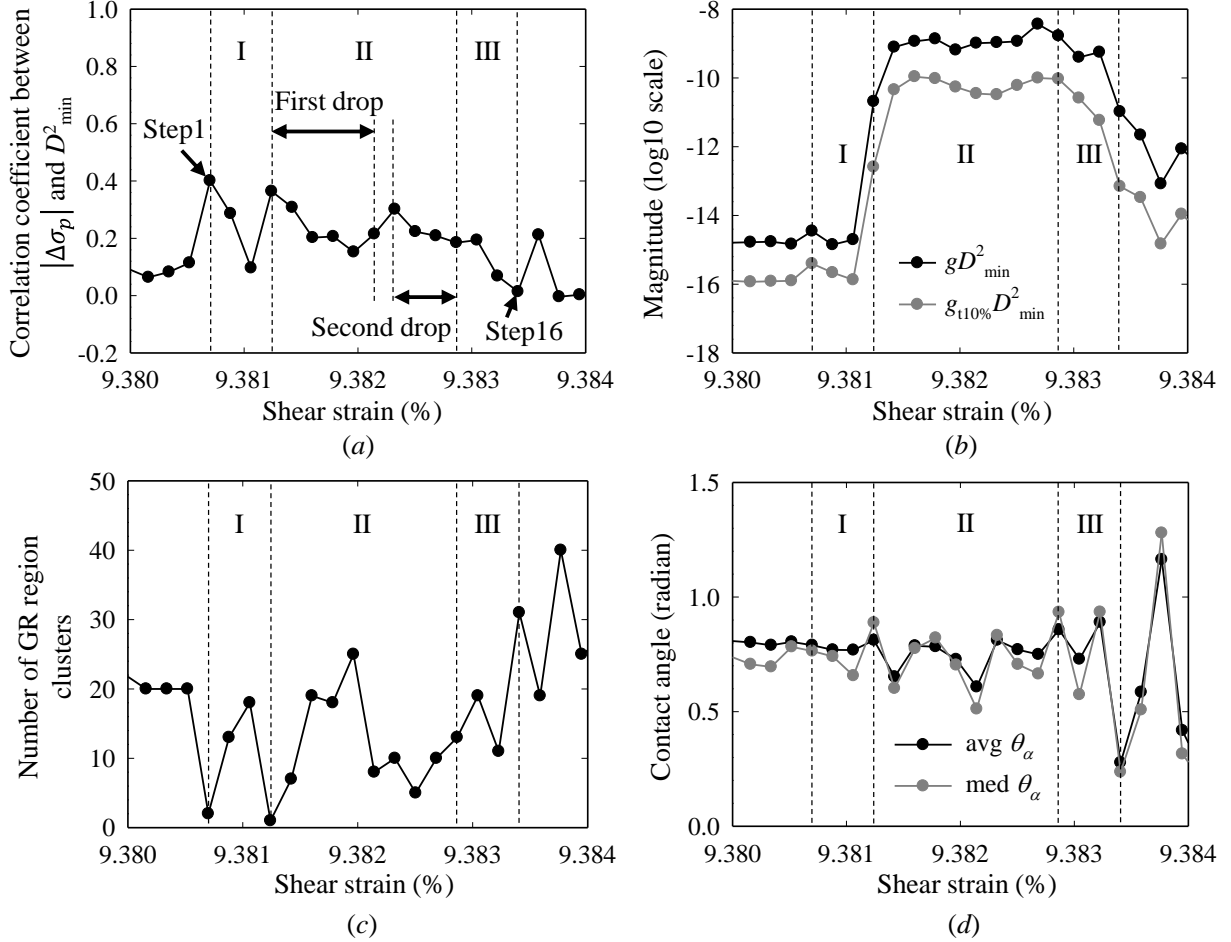


Fig. 21. (a) The Spearman correlation coefficients between the absolute value of the maximum principal stress change at a particle, $|\Delta\sigma_p|$, and ΔD_{\min}^2 , (b) the greatest D_{\min}^2 and the average of greatest top 10% D_{\min}^2 , (c) the number of GR force chain clusters, and (d) the average and the median of the absolute values of the contact angles in the GR region during 9.380 to 9.384% sample shear strain in the simulation with a large number of particles. The first stress drop and the second stress drop are indicated.

Figure 22 illustrates the Spearman correlation coefficients between kinematic measures and $\Delta\tau$ or $\Delta\tau_p$ for simulations with a smaller and a larger number of particles, with each correlation represented by different colors, in the steady-state regime. Specifically: (a) shows the correlation coefficient between $\Delta\tau$ and $g_{t10\%}D_{\min}^2$ across all instantaneous timesteps, (b) depicts the correlation coefficient between $\Delta\tau_p$ and

$mg_{t10\%}D_{\min}^2$ for all phases, (c) displays the correlation coefficient between $\Delta\tau_p$ and $mg_{t10\%}D_{\min}^2$ for long (l) phases, where t_p is greater than $3\Delta\gamma$, (d) shows the correlation coefficient between $\Delta\tau_p$ and $mg_{t10\%}D_{\min}^2$ for short (s) phases, where t_p is less than or equal to $3\Delta\gamma$, (e) displays the correlation coefficient between $\Delta\tau_p$ and mgD_{\min}^2 for long (l) phases, where t_p is greater than $3\Delta\gamma$, (f) depicts the correlation coefficient between $\Delta\tau_p$ and $sg_{t10\%}D_{\min}^2$ for all phases, (g) displays the correlation coefficient between $\Delta\tau_p$ and $sg_{t10\%}D_{\min}^2$ for long (l) phases, where t_p is greater than $3\Delta\gamma$, (h) shows the correlation coefficient between $\Delta\tau_p$ and $sg_{t10\%}D_{\min}^2$ for short (s) phases, where t_p is less than or equal to $3\Delta\gamma$, (i) displays the correlation coefficient between $\Delta\tau_p$ and sgD_{\min}^2 for long (l) phases, where t_p is greater than $3\Delta\gamma$, and (j) shows the correlation coefficient between $\Delta\tau_p$ and t_p for long (l) phases, where t_p is greater than $3\Delta\gamma$.

Figure 22a-i demonstrates consistent trends in the correlations between $\Delta\tau$ and $g_{t10\%}D_{\min}^2$ across all instantaneous timesteps and between $\Delta\tau_p$ and both $mg_{t10\%}D_{\min}^2$ and $sg_{t10\%}D_{\min}^2$ for all phases, long phases, and short phases, for the simulations with the different number of particles. Figure 22a-b and f shows that the correlations between $\Delta\tau_p$ and both $mg_{t10\%}D_{\min}^2$ and $sg_{t10\%}D_{\min}^2$ for the slip events ($\Delta\tau_p < 0$) across all phases mostly have stronger associations compared to those of $\Delta\tau$ with $g_{t10\%}D_{\min}^2$ across all instantaneous timesteps for $\Delta\tau < 0$ in both simulations. These stronger correlations observed for all phases, rather than at individual timesteps, indicate that analyzing the microscopic dynamics over the duration of a phase provides a better understanding of the macroscale responses of granular materials in both simulations. Figure 22b-c and f-g shows that $\Delta\tau_p - mg_{t10\%}D_{\min}^2$ and $\Delta\tau_p - sg_{t10\%}D_{\min}^2$ in long phases not only follow the same trend as those observed in all phases but also are mostly more highly correlated during the slip events ($\Delta\tau_p < 0$) in both simulations. The correlations between $\Delta\tau_p$ and both $mg_{t10\%}D_{\min}^2$ and $sg_{t10\%}D_{\min}^2$ for long phases are strong for a significant decrease in $\Delta\tau_p$ ($\Delta\tau_p < -10^{-2}$) and mostly moderate for a small decrease in $\Delta\tau_p$ ($10^{-2} < \Delta\tau_p < 0$) in both simulations. On the other hand, Figure 22d and h indicates that $\Delta\tau_p - mg_{t10\%}D_{\min}^2$ and $\Delta\tau_p - sg_{t10\%}D_{\min}^2$ in short phases do not exhibit strong correlations across all $\Delta\tau_p$ regimes in both simulations. This can be attributed to the fluctuations during short phases as shown in Stage III of Figures 14b, particularly when the structure is unstable. Figure 22c, e, g, and i shows that the correlations between $\Delta\tau_p$ and both $mg_{t10\%}D_{\min}^2$ and $sg_{t10\%}D_{\min}^2$ for long phases are consistently stronger than those between $\Delta\tau_p$ and both mgD_{\min}^2 and sgD_{\min}^2 during the slip events ($\Delta\tau_p < 0$), indicating that the variation in D_{\min}^2 values of particles around the one with the greatest D_{\min}^2 value has some effect on $\Delta\tau_p$ in both simulations. Figure 22c and g shows that during the slip events ($\Delta\tau_p < 0$), the correlations between $\Delta\tau_p$ and $sg_{t10\%}D_{\min}^2$ are almost equal to or stronger than those between $\Delta\tau_p$ and $mg_{t10\%}D_{\min}^2$ in long phases in both simulations. This implies that the phenomenon is history-dependent in both simulations, given that $sg_{t10\%}D_{\min}^2$ represents the

overall behavior of particle rearrangements during a slip event.

Figure 22j illustrates varying trends in the correlation between $\Delta\tau_p$ and t_p for long phases in both simulations. The results show that $\Delta\tau_p - t_p$ is mostly moderately correlated for large $\Delta\tau_p$ values ($\Delta\tau_p > 10^{-4}$) in the long stick events in both simulations. Unlike in the slip events, the structure of a sample during the stick events remains stable, showing low gD_{\min}^2 values for long phases, and as a result, τ_p increases gradually with an increase in t_p . On the other hand, $\Delta\tau_p - t_p$ is weakly correlated for small $\Delta\tau_p$ values ($-10^{-1} < \Delta\tau_p < -10^{-4}$) in long phases in both simulations because particle rearrangement is dominant during the long slip events. Appendix C includes the graphs for these correlation analyses with various sliding friction coefficients for the simulations with a larger number of particles (see Fig. 25), and they also follow the same trends.

In the simulation with a larger number of particles, compared to the simulation with a smaller number of particles, the number of minimum clusters of the GR regions during a slip event, N_c , is generally greater (Figs. 8c and 21c). Therefore, we measured the absolute values of the Spearman correlation coefficients of $\Delta\tau_p$ with N_c across various ranges of $mg_{t10\%}D_{\min}^2$ and $sg_{t10\%}D_{\min}^2$, respectively, during long phases in the steady-state regime. (Fig. 23). The results show that these absolute correlation coefficients are weak, indicating that N_c does not influence $\Delta\tau_p$ regardless of the values of $mg_{t10\%}D_{\min}^2$ and $sg_{t10\%}D_{\min}^2$ during long phases in the steady-state regime.

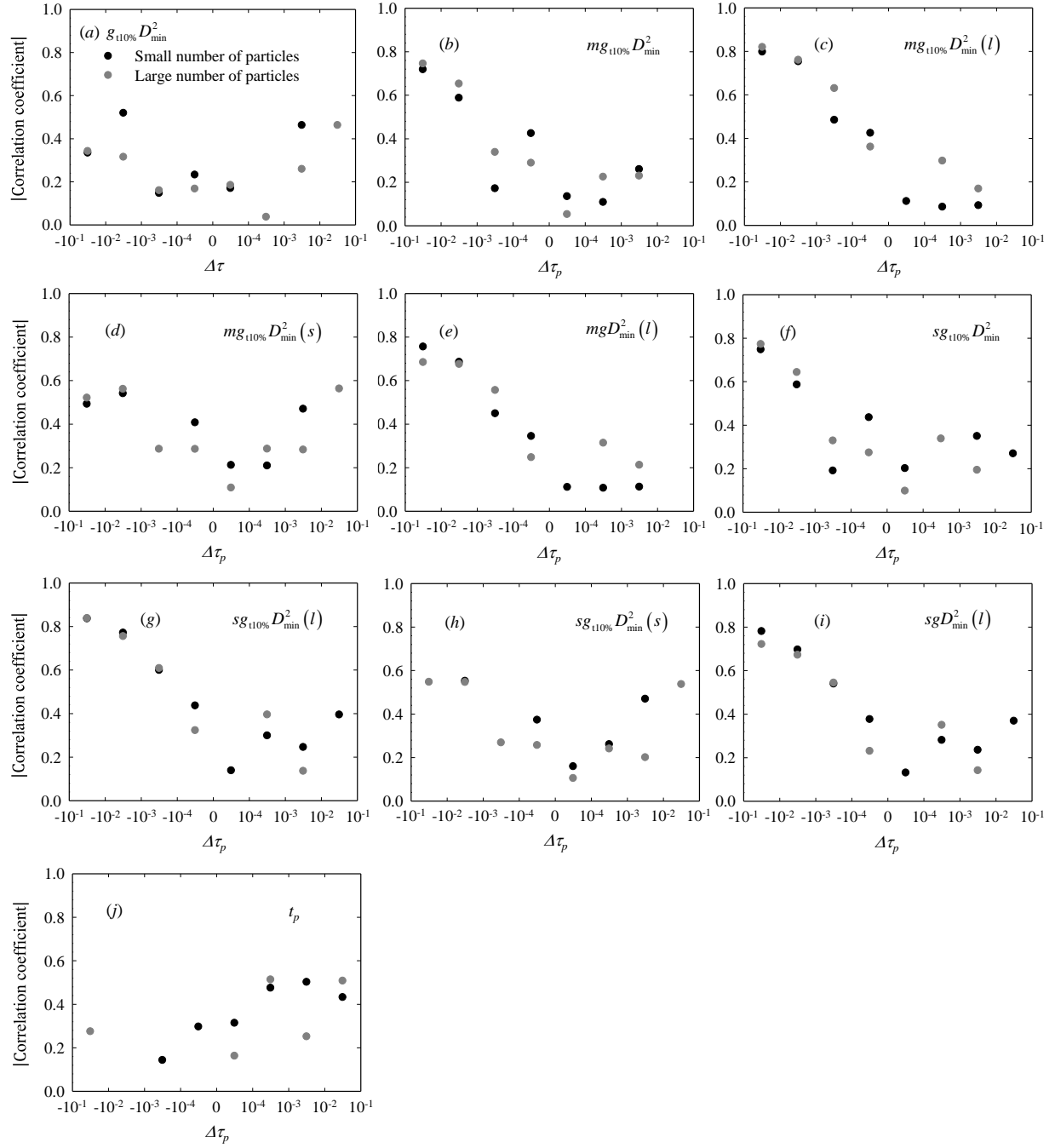


Fig. 22. Graphs of the absolute values of the Spearman correlation coefficients for between kinematic measures and $\Delta\tau$ or $\Delta\tau_p$ for simulations with a small and a large number of particles, with each represented by different colors, in the steady-state regime; (a) $\Delta\tau - g_{t10\%} D_{\min}^2$ across all instantaneous timesteps, (b) $\Delta\tau_p - mg_{t10\%} D_{\min}^2$ for all phases, (c) $\Delta\tau_p - mg_{t10\%} D_{\min}^2$ for long, l , ($> 3\Delta\gamma$) phases, (d) $\Delta\tau_p - mg_{t10\%} D_{\min}^2$ for short, s , ($\leq 3\Delta\gamma$) phases, (e) $\Delta\tau_p - mg D_{\min}^2$ for long, l , ($> 3\Delta\gamma$) phases, (f) $\Delta\tau_p - sg_{t10\%} D_{\min}^2$ for all phases, (g) $\Delta\tau_p - sg_{t10\%} D_{\min}^2$ for long, l , ($> 3\Delta\gamma$) phases, (h) $\Delta\tau_p - sg_{t10\%} D_{\min}^2$ for short, s , ($\leq 3\Delta\gamma$) phases, (i) $\Delta\tau_p - sg D_{\min}^2$ for long, l , ($> 3\Delta\gamma$) phases, and (j) $\Delta\tau_p - t_p$ for long, l , ($> 3\Delta\gamma$) phases.

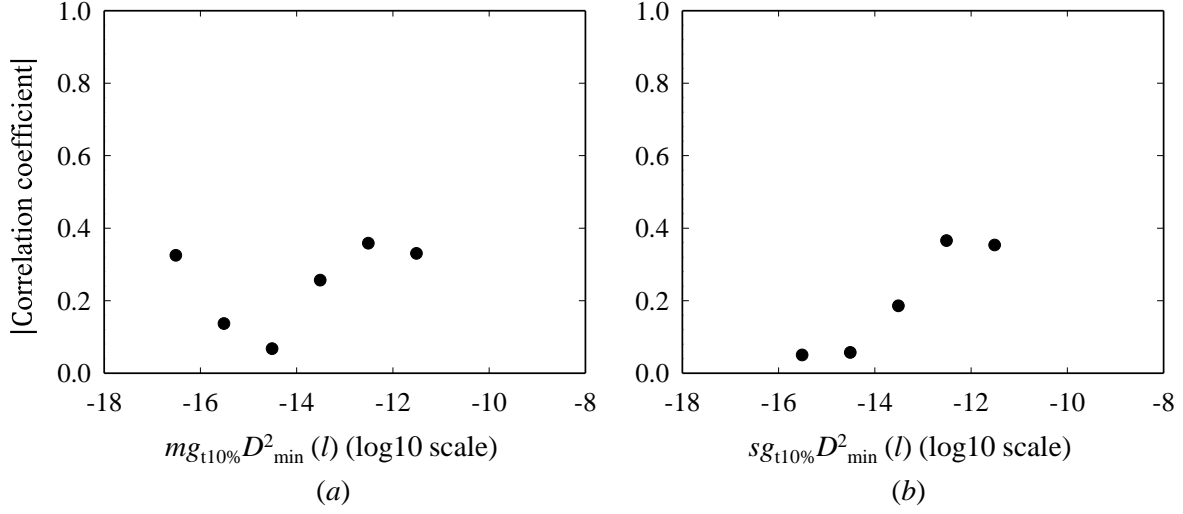


Fig. 23. The absolute values of the Spearman correlation coefficients between $\Delta\tau_p$ and with N_c across various ranges of (a) $mg_{t10\%} D^2_{\min}$ and (b) $sg_{t10\%} D^2_{\min}$, respectively, during long phases in the steady-state regime.

6. Discussion

In this study, we explored the relationship between microscopic dynamics and the differential force network around the slip event of a plane shear process for a granular material. In the pre-stress drop stage, there was no observable trend between microscopic dynamics and differential force network. During the stress drop stage, a single GR region was established, leading to particle rearrangement due to the weakening of the GR region and, consequently, a macroscale stress drop. In the post-stress drop stage, although macroscale stress fluctuated less, the microstructure remained unstable, and this fluctuation was short-lived.

Statistical analysis has deepened our understanding of the particle-scale mechanisms that contribute to macroscale stress decrease. During the slip event, we found a significant correlation between macroscale stress reduction and the greatest D^2_{\min} value, which is observed around the single clustered GR region. This strong correlation is due to the spatial clustering of microscopic dynamics and the large fluctuations in the differential force network. Furthermore, the variability in the D^2_{\min} values of the particles immediately surrounding the one with the greatest D^2_{\min} showed a correlation with the decrease in macroscale stress. This suggests that the magnitude of non-affine deformation in clustered STZs, rather than in a single STZ, influences the macroscale response in granular materials. It should be noted that these clustered STZs do not arise from multiple local STZs propagating but rather propagate from a single STZ that has the greatest D^2_{\min} value. Thus, in a mesoscale EPM, the magnitude of non-affine deformation of clustered STZs rather

than a single STZ should be considered as a point-like localized plastic event. We also found that, in our plane shear test, local shear transformation exhibited a nonlinear displacement field with either quadrupolar symmetry or a vortex shape. Therefore, this characteristic of the shear transformation zone should be accounted for in the elastic propagator of a mesoscale EPM. This comprehensive analysis underscores the interplay between microscopic dynamics and the differential force network with the macroscale stress responses, highlighting the critical need to integrate these mechanisms into a mesoscale EPM for granular materials.

7. Conclusions

We examined the microscopic dynamics of particle rearrangements during stick-slip behavior through force network analysis in plane shear simulations of granular materials. During slip events, particle rearrangement originates from the weakening of a clustered GR region – a region with the greatest reduction of inter-particle force magnitudes. From our statistical analysis, we found that the magnitude of the greatest non-affine deformation near the clustered GR region is highly correlated with the macroscale shear stress drop. In addition, the structure of neighboring particles of that point influences the macroscale shear stress drop. This trend persists in simulations with various sliding friction coefficients and a larger number of particles. The quantity and configuration of GR regions have minimal impact on macroscale stress drops. We expect our findings will provide an improved framework for validating and extending mesoscale elastoplastic models that are commonly used to explain mechanical behavior in amorphous and granular materials.

Acknowledgements

This research was supported by the U.S. National Science Foundation CAREER Grant No. CBET-1942096. The authors also gratefully acknowledge partial support from the U.S. Geological Survey Earthquake Hazards Program through Award No. G23AP00268.

References

- Ai, J., Chen, J. F., Rotter, J. M., & Ooi, J. Y. (2011). Assessment of rolling resistance models in discrete element simulations. *Powder Technology*, 206(3), 269-282.
- Argon, A. S. (1979). Plastic deformation in metallic glasses. *Acta metallurgica*, 27(1), 47-58.
- Barbot, A., Lerbinger, M., Hernandez-Garcia, A., García-García, R., Falk, M. L., Vandembroucq, D., & Patinet, S. (2018). Local yield stress statistics in model amorphous solids. *Physical Review E*, 97(3), 033001.

- Bardet, J. P., & Huang, Q. (1993). Rotational stiffness of cylindrical particle contacts. *Proceedings of the 2nd International Conference on Micromechanics of Granular Media*. Birmingham, UK, C. Thornton, ed., 39-44.
- Bretz, P., Kondic, L., & Kramar, M. (2023). Stochastic methods for slip prediction in a sheared granular system. *Physical Review E*, 107(5), 054901.
- Cates, M. E., Wittmer, J. P., Bouchaud, J. P., & Claudin, P. (1998). Jamming, force chains, and fragile matter. *Physical Review Letters*, 81(9), 1841.
- Cubuk, E. D., Schoenholz, S. S., Rieser, J. M., Malone, B. D., Rottler, J., Durian, D. J., ... & Liu, A. J. (2015). Identifying structural flow defects in disordered solids using machine-learning methods. *Physical Review Letters*, 114(10), 108001.
- Cubuk, E. D., Ivancic, R. J. S., Schoenholz, S. S., Strickland, D. J., Basu, A., Davidson, Z. S., ... & Liu, A. J. (2017). Structure-property relationships from universal signatures of plasticity in disordered solids. *Science*, 358(6366), 1033-1037.
- Da Cruz, F., Emam, S., Prochnow, M., Roux, J. N., & Chevoir, F. (2005). Rheophysics of dense granular materials: Discrete simulation of plane shear flows. *Physical Review E*, 72(2), 021309.
- Di Renzo, A., & Di Maio, F. P. (2005). An improved integral non-linear model for the contact of particles in distinct element simulations. *Chemical Engineering Science*, 60(5), 1303-1312.
- Falk, M. L., & Langer, J. S. (1998). Dynamics of viscoplastic deformation in amorphous solids. *Physical Review E*, 57(6), 7192.
- Hieronymus-Schmidt, V., Rösner, H., Wilde, G., & Zaccone, A. (2017). Shear banding in metallic glasses described by alignments of Eshelby quadrupoles. *Physical Review B*, 95(13), 134111.
- Hu, G., Hu, Z., Jian, B., Liu, L., & Wan, H. (2010, August). On the determination of the damping coefficient of non-linear spring-dashpot system to model hertz contact for simulation by discrete element method. *In 2010 WASE International Conference on Information Engineering* (Vol. 3, pp. 295-298). IEEE.
- Johnson, K. L. (1985). *Contact mechanics*. Cambridge university press.
- Kloss, C., Goniva, C., Hager, A., Amberger, S., & Pirker, S. (2012). Models, algorithms and validation for opensource DEM and CFD-DEM. *Progress in Computational Fluid Dynamics, an International Journal*, 12(2-3), 140-152.
- Kramár, M., Cheng, C., Basak, R., & Kondic, L. (2022). On intermittency in sheared granular systems. *Soft Matter*, 18(18), 3583-3593.
- Lai, Z., Chen, Q., & Huang, L. (2021). A semianalytical Hertzian frictional contact model in 2D. *Applied Mathematical Modelling*, 92, 546-564.
- Langer, J. S. (2001). Microstructural shear localization in plastic deformation of amorphous solids. *Physical*

- Review E*, 64(1), 011504.
- Ma, G., Zou, Y., Chen, Y., Tang, L., Ng, T. T., & Zhou, W. (2021). Spatial correlation and temporal evolution of plastic heterogeneity in sheared granular materials. *Powder Technology*, 378, 263-273.
- Ma, G., Mei, J., Gao, K., Zhao, J., Zhou, W., & Wang, D. (2022). Machine learning bridges microslips and slip avalanches of sheared granular gouges. *Earth and Planetary Science Letters*, 579, 117366.
- Mei, J., Ma, G., Wang, Q., Wu, T., & Zhou, W. (2022). Micro-and macroscopic aspects of the intermittent behaviors of granular materials related by graph neural network. *International Journal of Solids and Structures*, 251, 111763.
- Mei, J., Ma, G., Tang, L., Gao, K., Cao, W., & Zhou, W. (2023). Spatial clustering of microscopic dynamics governs the slip avalanche of sheared granular materials. *International Journal of Plasticity*, 163, 103570.
- Nicolas, A., Ferrero, E. E., Martens, K., & Barrat, J. L. (2018). Deformation and flow of amorphous solids: Insights from elastoplastic models. *Reviews of Modern Physics*, 90(4), 045006.
- Patinet, S., Vandembroucq, D., & Falk, M. L. (2016). Connecting local yield stresses with plastic activity in amorphous solids. *Physical Review Letters*, 117(4), 045501.
- Peters, J. F., Muthuswamy, M., Wibowo, J., & Tordesillas, A. (2005). Characterization of force chains in granular material. *Physical Review E*, 72(4), 041307.
- Picard, G., Ajdari, A., Lequeux, F., & Bocquet, L. (2004). Elastic consequences of a single plastic event: A step towards the microscopic modeling of the flow of yield stress fluids. *The European Physical Journal E*, 15, 371-381.
- Picard, G., Ajdari, A., Lequeux, F., & Bocquet, L. (2005). Slow flows of yield stress fluids: Complex spatiotemporal behavior within a simple elastoplastic model. *Physical Review E*, 71(1), 010501.
- Radjai, F., Wolf, D. E., Jean, M., & Moreau, J. J. (1998). Bimodal character of stress transmission in granular packings. *Physical Review Letters*, 80(1), 61.
- Richard, D., Ozawa, M., Patinet, S., Stanifer, E., Shang, B., Ridout, S. A., ... & Manning, M. L. (2020). Predicting plasticity in disordered solids from structural indicators. *Physical Review Materials*, 4(11), 113609.
- Ruan, D., Patinet, S., & Falk, M. L. (2022). Predicting plastic events and quantifying the local yield surface in 3D model glasses. *Journal of the Mechanics and Physics of Solids*, 158, 104671.
- Shi, R. H., Wu, Y. C., Shuang, F., & Zhang, Z. W. (2023). Dipolar and quadrupolar characteristics of shear transformation in two dimensional metallic glasses. *Materials Today Communications*, 34, 105389.
- Spaepen, F. (1977). A microscopic mechanism for steady state inhomogeneous flow in metallic glasses. *Acta Metallurgica*, 25(4), 407-415.
- Stanifer, E., & Manning, M. L. (2022). Avalanche dynamics in sheared athermal particle packings occurs

- via localized bursts predicted by unstable linear response. *Soft Matter*, 18(12), 2394-2406.
- Steif, P. S., Spaepen, F., & Hutchinson, J. W. (1982). Strain localization in amorphous metals. *Acta Metallurgica*, 30(2), 447-455.
- Tordesillas, A. (2007). Force chain buckling, unjamming transitions and shear banding in dense granular assemblies. *Philosophical Magazine*, 87(32), 4987-5016.
- Tordesillas, A., & Muthuswamy, M. (2008). A thermomicromechanical approach to multiscale continuum modeling of dense granular materials. *Acta Geotechnica*, 3, 225-240.
- Tordesillas, A., & Muthuswamy, M. (2009). On the modeling of confined buckling of force chains. *Journal of the Mechanics and Physics of Solids*, 57(4), 706-727.
- Tordesillas, A., Lin, Q., Zhang, J., Behringer, R. P., & Shi, J. (2011). Structural stability and jamming of self-organized cluster conformations in dense granular materials. *Journal of the Mechanics and Physics of Solids*, 59(2), 265-296.
- Xu, B., Falk, M. L., Patinet, S., & Guan, P. (2021). Atomic nonaffinity as a predictor of plasticity in amorphous solids. *Physical Review Materials*, 5(2), 025603.
- Zabulionis, D., Kacianauskas, R., Markauskas, D., & Rojek, J. (2012). An investigation of nonlinear tangential contact behaviour of a spherical particle under varying loading. *Bulletin of the Polish Academy of Sciences. Technical Sciences*, 60(2), 265-278.
- Zhai, C., Albayrak, N., Engqvist, J., Hall, S. A., Wright, J., Majkut, M., ... & Hurley, R. C. (2022). Quantifying local rearrangements in three-dimensional granular materials: Rearrangement measures, correlations, and relationship to stresses. *Physical Review E*, 105(1), 014904.

Appendix

A. Contact models

The normal contact force, F_n , consists of the normal elastic repulsive force, F_n^e , and the normal damping force, F_n^d , as

$$F_n = F_n^e + F_n^d = k_n \delta_n + \gamma_n \dot{\delta}_n \quad (\text{A1})$$

where k_n is the normal contact stiffness, δ_n is the normal overlapped displacement, γ_n is the viscoelastic damping constant for the normal contact force, and $\dot{\delta}_n$ is the normal relative velocity between the two particles. The k_n for cylindrical bodies can be calculated as (Johnson, 1985)

$$k_n = \pi E^* [\log(4R_1/a) + \log(4R_2/a) - 1]^{-1} \quad (\text{A2})$$

$$\frac{1}{E^*} = \frac{1 - \nu_1^2}{E_1} + \frac{1 - \nu_2^2}{E_2} \quad (\text{A3})$$

where R_1 and R_2 are the radius of particles 1 and 2, respectively, a is the radius of contact area, E_1 and E_2 are Young's modulus of particles 1 and 2, respectively, and ν_1 and ν_2 are Poisson's ratio of particles 1 and 2, respectively. By using the linear damping model (Hu *et al.*, 2011), the γ_n can be calculated as

$$\gamma_n = 2\alpha \sqrt{k_n m^*} \quad (\text{A4})$$

$$\frac{1}{m^*} = \frac{1}{m_1} + \frac{1}{m_2} \quad (\text{A5})$$

where α is the damping ratio without dimension, and m_1 and m_2 are the mass of particles 1 and 2, respectively.

The tangential contact force, F_t , consists of the tangential elastic repulsive force, F_t^e , and the tangential damping force, F_t^d , as

$$F_t = F_t^e + F_t^d \quad (\text{A6})$$

To consider the effects of various normal contact forces, F_t^e is incrementally calculated as (Di Renzo and Di Maio, 2005; Lai *et al.*, 2021)

$$F_t^e = F_t^0 + k_t \Delta \delta_t \quad (\text{A7})$$

where F_t^0 is the tangential contact force at the previous time step, k_t is the tangential contact stiffness, δ_t is

the tangential overlapped displacement, and $\Delta\delta_t$ is the incremental tangential overlapped displacement. By using Lai *et al.*'s semi-analytical Hertzian frictional contact model in two dimensions (2021), k_t can be calculated as

$$k_t = \pi E^* \left[\log(2R_1 / a) + \log(2R_2 / a) + 1 + w_1^{(a)} (\log(4R_1 / a) + \nu_1 / 2(1 - \nu_1)) + w_2^{(a)} (\log(4R_2 / a) + \nu_2 / 2(1 - \nu_2)) \right]^{-1} \quad (\text{A8})$$

Here, $w_1^{(a)}$ and $w_2^{(a)}$ are the penalty factors, which can be calculated as

$$\begin{aligned} w_1^{(a)} &= 0.22 + 2.89(a / R_1) + 0.18\nu_1 - 10.31(a / R_1)^2 + 1.75(a / R_1)\nu_1 + 0.36\nu_1^2 \\ w_2^{(a)} &= 0.22 + 2.89(a / R_2) + 0.18\nu_2 - 10.31(a / R_2)^2 + 1.75(a / R_2)\nu_2 + 0.36\nu_2^2 \end{aligned} \quad (\text{A9})$$

The tangential elastic repulsive force, F_t^e , calculated in Eq. (A7) is subjected to Coulomb's law of friction as

$$F_t^e = \min(F_t^0 + k_t \Delta\delta_t, \mu_s F_n) \quad (\text{A10})$$

where μ_s is the sliding friction coefficient.

The tangential damping force, F_t^d , is calculated as

$$F_t^d = \gamma_t \dot{\delta}_t \quad (\text{A11})$$

where γ_t is the viscoelastic damping constant for tangential force, and $\dot{\delta}_t$ is the tangential relative velocity between the two particles. By using the linear damping model (Hu *et al.*, 2011), the γ_t can be calculated as

$$\gamma_t = 2\alpha \sqrt{k_t m^*} \quad (\text{A12})$$

In the type C elasto-plastic spring-dashpot models (Ai *et al.*, 2011), the total rolling resistance torque, M_r , consists of a spring torque, M_r^k , and a viscous damping torque, M_r^d , as

$$M_r = M_r^k + M_r^d \quad (\text{A13})$$

This model can be implemented in a computer program in an incremental manner. The incremental spring torque, ΔM_r^k , is calculated from the incremental relative rotation between two particles, $\Delta\theta_r$, and the rolling stiffness, k_r , as

$$\Delta M_r^k = -k_r \Delta \theta_r \quad (\text{A14})$$

where k_r is calculated as (Bardet and Huang, 1993)

$$k_r = \frac{\pi E^* R_r^2}{4} \quad (\text{A15})$$

$$\frac{1}{R_r} = \frac{1}{R_1} + \frac{1}{R_2} \quad (\text{A16})$$

If the spring torque at time t is $M_{r,t}^k$, the spring torque at time $t + \Delta t$ is given as

$$\begin{cases} M_{r,t+\Delta t}^k = M_{r,t}^k + \Delta M_r^k \\ |M_{r,t+\Delta t}^k| \leq M_r^m \end{cases} \quad (\text{A17})$$

where M_r^m is the limiting spring torque calculated as

$$M_r^m = \mu_r R_r F_n \quad (\text{A18})$$

Here, μ_r is the rolling friction coefficients.

The viscous damping torque M_r^d is assumed to be dependent on the relative rolling angular velocity, $\Delta \dot{\theta}_r$, between the two particles in contact and the rolling viscous damping constant, C_r , such that

$$M_{r,t+\Delta t}^d = \begin{cases} -C_r \dot{\theta}_r & \text{if } |M_{r,t+\Delta t}^d| < M_r^m \\ 0 & \text{if } |M_{r,t+\Delta t}^d| = M_r^m \end{cases} \quad (\text{A19})$$

The C_r is expressed as

$$C_r = \eta_r C_r^{\text{crit}} \quad (\text{A20})$$

where η_r is the rolling viscous damping ratio and C_r^{crit} is the rolling critical viscous damping constant calculated as

$$C_r^{\text{crit}} = 2\sqrt{I_r k_r} \quad (\text{A21})$$

in which I_r is the equivalent moment of inertia for the relative rotational vibration model about the contact point between the two contacting disks expressed as

$$\frac{1}{I_r} = \frac{1}{I_1 + m_1 R_1^2} + \frac{1}{I_2 + m_2 R_2^2} \quad (\text{A22})$$

where I_1 and I_2 are the moments of inertia of particles 1 and 2, respectively, with respect to their own centroids.

In DEM simulation, to prevent an artificial jump in the elastic tangential overlapped displacement vector, δ_t , δ_t is updated as (Zabulionis *et al.*, 2012)

$$\delta_t(t_i) = \begin{cases} \delta_t(t_{i-1}) + \mathbf{v}_{c,t}(t_i)(t_i - t_{i-1}) & \text{when } \mathbf{F}_t(t_i) \leq \mu \|\mathbf{F}_n(t_i)\| \\ \delta_t(t_{i-1}) - \frac{1}{k_t(t_i)} (\mathbf{t} \mu_s \|\mathbf{F}_n(t_i)\| - \mu \mathbf{F}_t(t_{i-1})) & \text{when } \mathbf{F}_t(t_i) > \mu \|\mathbf{F}_n(t_i)\| \end{cases} \quad (\text{A23})$$

where t_i and t_{i-1} are the time steps at i and $i-1$, respectively, $\mathbf{v}_{c,t}$ is the tangential component of the relative velocity vector at the contact point of the particles, \mathbf{t} is the unit vector of the tangential interaction, \mathbf{F}_n is the normal contact force vector, and \mathbf{F}_t is the tangential contact force vector.

B. D^2_{\min} Computation

As described in the main text, the D^2_{\min} is a measure of the magnitude of the local non-affine deformation. Specifically, D^2_{\min} calculates the mean-square difference between the actual displacements of neighboring particles in the local averaging region relative to a central particle and the displacements that would occur if they were in a uniformly deformed region described by a local affine tensor, $\mathbf{\Gamma}$. The local averaging regions are defined as regions of radius $r = N r_p$, where N is an integer, centered on the center of mass of a particle with average radius r_p . Therefore, with a given strain increment at the scale of the system, $\Delta\gamma$, the D^2_{\min} for a specific particle i can be calculated as (Mei *et al.*, 2023).

$$D^2_{\min}(\gamma, \Delta\gamma) = \frac{1}{N_i} \sum_j^{N_i} \left\{ \mathbf{r}_j(\gamma) - \mathbf{r}_i(\gamma) - \mathbf{\Gamma} [\mathbf{r}_j(\gamma - \Delta\gamma) - \mathbf{r}_i(\gamma - \Delta\gamma)] \right\}^2 \quad (\text{B1})$$

where γ is the macroscopic shear strain of a given time, N_i is the number of the neighbor particles of the particle i within a local average region, and j represents the neighboring particles of the particle i . At a given strain, $\gamma - \Delta\gamma$, particles j that surround the particle i are defined to form its neighborhood. $\mathbf{r}_i(\gamma)$ and $\mathbf{r}_j(\gamma)$ are the vectors from the origin of coordinate systems to the location of the particles i and j at a given strain, γ , respectively. The locally best-fit affine tensor, $\mathbf{\Gamma}$, can be obtained by minimizing the quantity D^2_{\min} as (Falk and Langer, 1998)

$$\mathbf{X} = \sum_j^{N_i} [\mathbf{r}_j(\gamma) - \mathbf{r}_i(\gamma)] \otimes [\mathbf{r}_j(\gamma - \Delta\gamma) - \mathbf{r}_i(\gamma - \Delta\gamma)] \quad (\text{B2})$$

$$\mathbf{Y} = \sum_j^{N_i} [\mathbf{r}_j(\gamma - \Delta\gamma) - \mathbf{r}_i(\gamma - \Delta\gamma)] \otimes [\mathbf{r}_j(\gamma - \Delta\gamma) - \mathbf{r}_i(\gamma - \Delta\gamma)] \quad (\text{B3})$$

$$\mathbf{\Gamma} = \mathbf{X} \cdot \mathbf{Y}^{-1} \quad (\text{B4})$$

C. DEM results for the simulation with a large number of particles

In this section, DEM results for the simulation with a large number of particles are presented. Figure 24 displays the normalized shear stress-strain curves for various sliding friction coefficients for the simulation with a large number of particles. Employing a dataset that includes approximately 130,000 timesteps for each of the four simulations with sliding friction coefficients ($\mu_s = 0.1, 0.3, 0.5$, and 0.7), we observed approximately 12,000 phases for $\mu_s = 0.1$, 31,000 for $\mu_s = 0.3$, 31,000 for $\mu_s = 0.5$, and 26,000 for $\mu_s = 0.7$ within the steady-state regime. We examined the correlations between various parameters and $\Delta\tau$ across these timesteps and phases. Figure 25 illustrates the absolute values of the Spearman correlation coefficients between kinematic measures and $\Delta\tau$ or $\Delta\tau_p$ for various sliding friction coefficients, with each value of μ_s represented by different symbols, in the steady-state regime for the simulation with a large number of particles. Specifically: (a) shows the correlation coefficient between $\Delta\tau$ and $g_{t10\%}D_{\min}^2$ across all instantaneous timesteps, or equivalently, across strain intervals of $\Delta\gamma = 1.8 \times 10^{-6}$, (b) depicts the correlation coefficient between $\Delta\tau_p$ and $mg_{t10\%}D_{\min}^2$ for all phases, (c) displays the correlation coefficient between $\Delta\tau_p$ and $mg_{t10\%}D_{\min}^2$ for long (l) phases, where t_p is greater than $3\Delta\gamma$, (d) shows the correlation coefficient between $\Delta\tau_p$ and $mg_{t10\%}D_{\min}^2$ for short (s) phases, where t_p is less than or equal to $3\Delta\gamma$, (e) displays the correlation coefficient between $\Delta\tau_p$ and mgD_{\min}^2 for long (l) phases, where t_p is greater than $3\Delta\gamma$, (f) depicts the correlation coefficient between $\Delta\tau_p$ and $sg_{t10\%}D_{\min}^2$ for all phases, (g) displays the correlation coefficient between $\Delta\tau_p$ and $sg_{t10\%}D_{\min}^2$ for long (l) phases, where t_p is greater than $3\Delta\gamma$, (h) shows the correlation coefficient between $\Delta\tau_p$ and $sg_{t10\%}D_{\min}^2$ for short (s) phases, where t_p is less than or equal to $3\Delta\gamma$, (i) displays the correlation coefficient between $\Delta\tau_p$ and sgD_{\min}^2 for long (l) phases, where t_p is greater than $3\Delta\gamma$, and (j) shows the correlation coefficient between $\Delta\tau_p$ and t_p for long (l) phases, where t_p is greater than $3\Delta\gamma$.

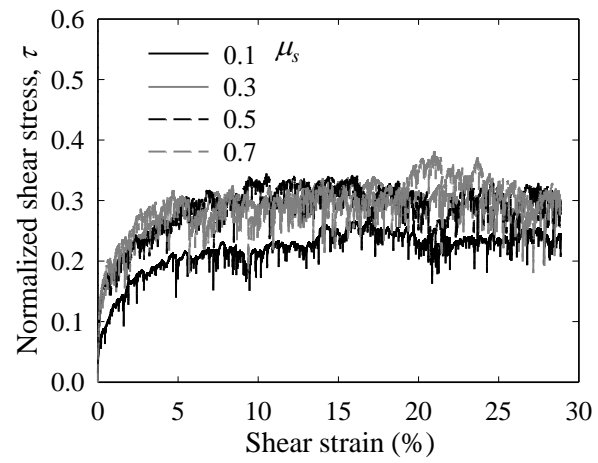


Fig. 24. Normalized shear stress-strain curve from discrete element method simulation with a large number of particles for various sliding friction coefficients.

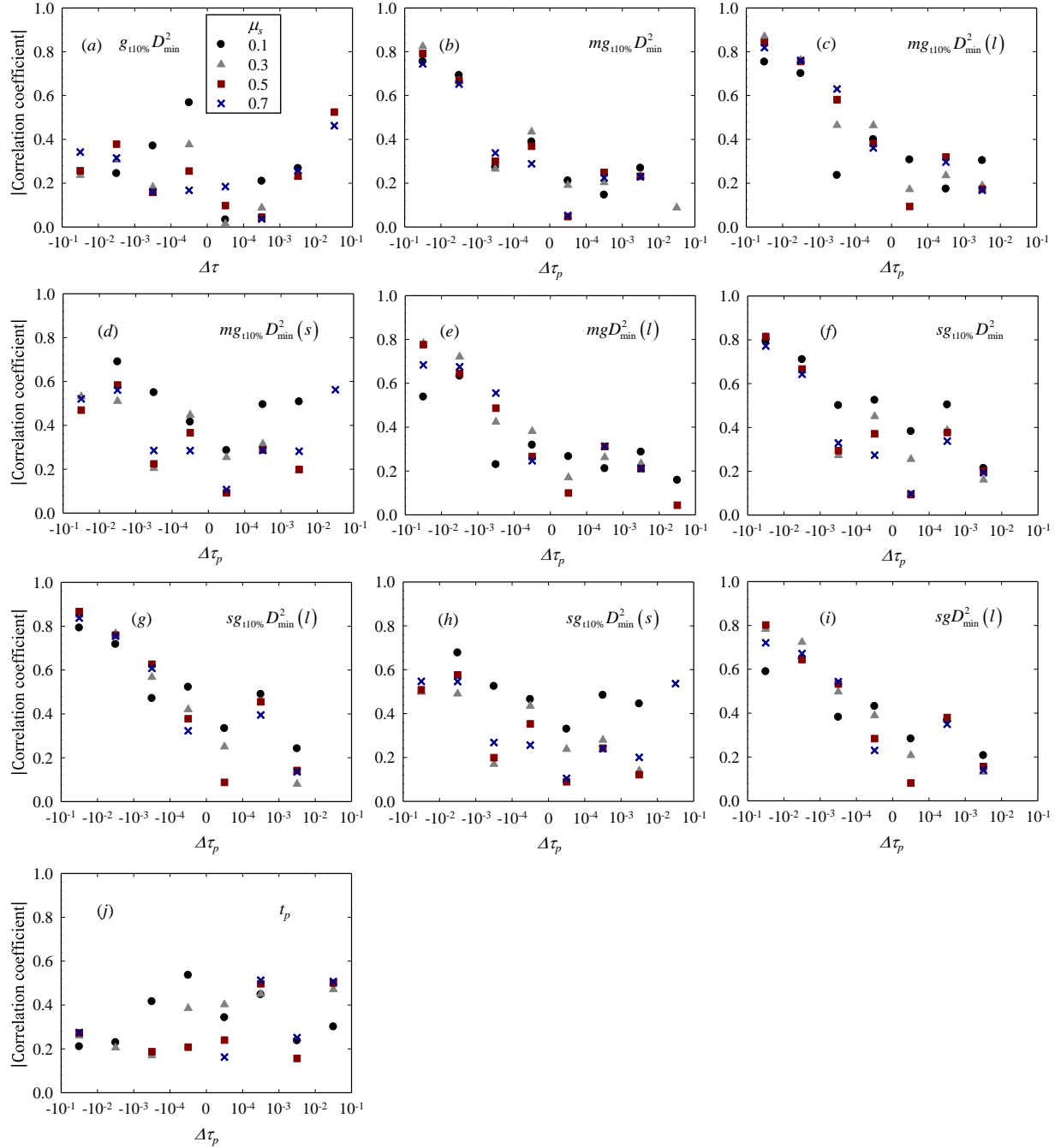


Fig. 25. Graphs of the absolute values of the Spearman correlation coefficients for between kinematic measures and $\Delta\tau$ or $\Delta\tau_p$ for various sliding friction coefficients, with each value of μ_s represented by different symbols, in the steady-state regime for the simulations with a large number of particles; (a) $\Delta\tau - g_{t10\%} D_{\min}^2$ across all instantaneous timesteps, (b) $\Delta\tau_p - mg_{t10\%} D_{\min}^2$ for all phases, (c) $\Delta\tau_p - mg_{t10\%} D_{\min}^2$ for long, l , ($> 3\Delta\gamma$) phases, (d) $\Delta\tau_p - mg_{t10\%} D_{\min}^2$ for short, s , ($\leq 3\Delta\gamma$) phases, (e) $\Delta\tau_p - mg D_{\min}^2$ for long, l , ($> 3\Delta\gamma$) phases, (f) $\Delta\tau_p - sg_{t10\%} D_{\min}^2$ for all phases, (g) $\Delta\tau_p - sg_{t10\%} D_{\min}^2$ for long, l , ($> 3\Delta\gamma$) phases, (h) $\Delta\tau_p - sg_{t10\%} D_{\min}^2$ for short, s , ($\leq 3\Delta\gamma$) phases, (i) $\Delta\tau_p - sg D_{\min}^2$ for long, l , ($> 3\Delta\gamma$) phases, and (j) $\Delta\tau_p - t_p$ for long, l , ($> 3\Delta\gamma$) phases.